The Astrophysical Journal, 997:250 (20pp), 2026 February 1 https://doi.org/10.3847/1538-4357/ae2681

Abundant Population of Broad Hα Emitters in the GOODS-N Field Revealed by CONGRESS, FRESCO, and JADES

Junyu Zhang[1], Eiichi Egami[1], Fengwu Sun[2], Xiaojing Lin[1,3], Jianwei Lyu[1], Yongda Zhu[1], Pierluigi Rinaldi[4], Yang Sun[1], Andrew J. Bunker[5], Rachana Bhatawdekar[6], Jakob M. Helton[7], Roberto Maiolino[8,9,10], Zheng Ma[1], Brant Robertson[11], Sandro Tacchella[8,12], Giacomo Venturi[13], Christina C. Williams[14], and Chris Willott[15]
[1] Steward Observatory, University of Arizona, 933 North Cherry Avenue, Tucson, AZ 85721, USA
[2] Center for Astrophysics | Harvard & Smithsonian, 60 Garden Street, Cambridge, MA 02138, USA
[3] Department of Astronomy, Tsinghua University, Beijing 100084, People's Republic of China
[4] Space Telescope Science Institute, 3700 San Martin Drive, Baltimore, MD 21218, USA
[5] Department of Physics, University of Oxford, Denys Wilkinson Building, Keble Road, Oxford OX1 3RH, UK
[6] European Space Agency (ESA), European Space Astronomy Centre (ESAC), Camino Bajo del Castillo s/n, 28692, Villanueva de la Cañada, Madrid, Spain
[7] Department of Astronomy & Astrophysics, The Pennsylvania State University, University Park, PA 16802, USA
[8] Kavli Institute for Cosmology, University of Cambridge, Madingley Road, Cambridge, CB3 0HA, UK
[9] Cavendish Laboratory—Astrophysics Group, University of Cambridge, 19 JJ Thomson Avenue, Cambridge, CB3 0HE, UK
[10] Department of Physics and Astronomy, University College London, Gower Street, London WC1E 6BT, UK
[11] Department of Astronomy and Astrophysics, University of California, Santa Cruz, 1156 High Street, Santa Cruz, CA 96054, USA
[12] Cavendish Laboratory, University of Cambridge, 19 JJ Thomson Avenue, Cambridge, CB3 0HE, UK
[13] Scuola Normale Superiore, Piazza dei Cavalieri 7, I-56126 Pisa, Italy
[14] NSF National Optical-Infrared Astronomy Research Laboratory, 950 North Cherry Avenue, Tucson, AZ 85719, USA
[15] NRC Herzberg, 5071 West Saanich Road, Victoria, BC V9E 2E7, Canada
Received 2025 May 5; revised 2025 November 20; accepted 2025 November 28; published 2026 January 27

Abstract

We present a spectroscopic search for broad Hα emitters at $z \approx 3.7$–6.5 in the GOODS-N field, utilizing JWST/NIRCam slitless spectroscopy from FRESCO and CONGRESS, complemented by JADES imaging. We identify 19 broad Hα emitters with FWHM $> 1000\,\mathrm{km\,s^{-1}}$ at $z \approx 4$–5.5, including nine new sources. The broad Hα luminosity function derived from our sample is consistent with those of other JWST-selected broad-line active galactic nuclei (AGN) reported in the literature. The black hole masses and AGN bolometric luminosities inferred from the broad Hα components indicate that most sources are accreting at ∼10% of the Eddington limit. We derive their host stellar masses via spectral energy distribution (SED) fitting and find higher $M_{\rm BH}/M_*$ ratios relative to the local $M_{\rm BH}$–M_* relations, consistent with previous studies. We find that 42% of the sample do not satisfy the widely used color selection criteria for little red dots (LRDs), with the majority of these sources lacking the characteristic steep rest-optical red slope, indicating that the LRD selection is highly incomplete when selecting AGN galaxies. A comparison of the average SEDs between our sample and LRDs selected in the same field reveals that the steep red slopes observed in some LRDs are likely due to line-boosting effects as previously suggested. Furthermore, we find that 68% of color-selected LRDs with Hα detections in the NIRCam/grism spectra do not exhibit broad-line features. While the limited sensitivity of the grism spectra may hinder the detection of broad-line components in faint sources, our findings still highlight the enigmatic nature of the LRD population.

Unified Astronomy Thesaurus concepts: AGN host galaxies (2017); Active galactic nuclei (16); Supermassive black holes (1663); High-redshift galaxies (734)

1. Introduction

Supermassive black holes (SMBHs) are thought to reside at the centers of most massive galaxies (J. Kormendy & L. C. Ho 2013; J. E. Greene et al. 2020). The efficient accretion processes associated with these SMBHs contribute to the formation of active galactic nuclei (AGN), causing their host galaxies to exhibit broadened emission line profiles compared to nonactive galaxies. Understanding the characteristics of AGN and accurately estimating their abundance in the early Universe ($z > 3$) are essential for addressing key questions in extragalactic astronomy, including the reionization of the Universe and the coevolution of AGN and their host galaxies.

Prior to the launch of the JWST (J. P. Gardner et al. 2023), studying the abundance and properties of faint AGN at high redshifts was highly challenging due to observational limitations. For AGN with ultraviolet (UV) magnitudes fainter than $M_{\rm UV} = -22$, determining their space density and physical properties was particularly difficult, with significant discrepancies reported (e.g., S. Parsa et al. 2018; E. Giallongo et al. 2019; T. Morishita et al. 2020; X. Shen et al. 2020; S. L. Finkelstein & M. B. Bagley 2022). The advent of JWST, with its unparalleled infrared sensitivity, has opened up new avenues for investigating these faint, distant objects. Recent JWST observations have demonstrated its remarkable capability to identify UV-faint AGN in the early Universe through various methodologies, including the detection of broad Balmer lines (Y. Harikane et al. 2023; D. D. Kocevski et al. 2023; R. L. Larson et al. 2023; P. A. Oesch et al. 2023; H. Übler et al. 2023; G. Barro et al. 2024; J. E. Greene et al. 2024;

R. Maiolino et al. 2024; J. Matthee et al. 2024; X. Lin et al. 2026).

Among the UV-faint AGN detected by JWST, an intriguing subset of the AGN population consists of sources with notably compact sizes and red colors. J. Matthee et al. (2024) assembled one of the earliest samples of these sources, identified through broad Hα emission lines, and named them "little red dots" (LRDs). These LRDs appear as point sources and exhibit distinctive spectral energy distributions (SEDs), characterized by blue rest-frame UV slopes and extremely steep red rest-frame optical slopes (e.g., J. E. Greene et al. 2024; A. de Graaff et al. 2025; X. Ji et al. 2025; I. Labbé et al. 2025; R. P. Naidu et al. 2025). Such a "V-shaped" SED is found to be rare for AGN at $z < 2$ (e.g., A. Noboriguchi et al. 2019). To investigate the origin of the UV and optical emission in LRDs, several recent studies have assembled samples of these objects by identifying compact sources and targeting those with "V-shaped" SEDs, using NIRCam color cuts as a selection criterion (H. B. Akins et al. 2023; G. Barro et al. 2024; J. E. Greene et al. 2024; V. Kokorev et al. 2024; P. G. Pérez-González et al. 2024; P. Rinaldi et al. 2025a; C. C. Williams et al. 2024; I. Labbé et al. 2025).

Although numerous photometrically selected LRD candidates have been assembled, their true nature remains uncertain. It is still unclear whether these LRDs are primarily AGN, in which the red optical continua arise from dust emission in front of UV-bright AGN (e.g., H. B. Akins et al. 2023; R. Maiolino et al. 2024) or nonstellar Balmer breaks (X. Lin et al. 2025b), or whether they are dusty star-forming galaxies, where strong emission lines such as Hα or [O III] with high equivalent widths can boost the broadband fluxes and make the rest-frame optical colors appear red (e.g., G. Barro et al. 2024; P. G. Pérez-González et al. 2024; R. E. Hviding et al. 2025). An additional possibility is that some LRDs may be "black hole stars" embedded in relatively bright host galaxies, in which extremely dense gas forms a dust-free atmosphere around an SMBH, producing strong Balmer break and absorption features (R. P. Naidu et al. 2025). J. E. Greene et al. (2024) obtained follow-up NIRSpec spectroscopy on 15 LRDs photometrically selected in I. Labbé et al. (2025) and found that 60% exhibited definitive evidence of broad Hα lines, confirming an AGN nature for a significant subset. In contrast, P. G. Pérez-González et al. (2024) reported that only 17% of their photometrically selected LRDs with available spectroscopy displayed broad-line features. However, this fraction may be underestimated, as many existing broad lines could not be confirmed due to insufficient signal-to-noise ratio (S/N) of the grism spectra (C. C. Williams et al. 2024). In P. Rinaldi et al. (2025a), analysis of the emission line properties of the LRD sample using NIRSpec spectra and classical line ratio diagnostics was unable to conclusively determine their nature, suggesting a likely mixed origin.

Furthermore, SED fitting results for these LRDs indicate that the origin of their red colors remains unclear. Although SED fits to LRDs with JWST and Atacama Large Millimeter/submillimeter Array (ALMA) observations favor models with dusty AGN over obscured star formation to explain their red optical colors, this does not completely rule out a stellar-dominated origin, as dust-obscured older stellar populations remain consistent with the ALMA limits (C. C. Williams et al. 2024; I. Labbé et al. 2025).

In this work, we utilize grism spectroscopic data from the First Reionization Epoch Spectroscopically Complete Observations (FRESCO-PID: 1895; PI: P. Oesch; P. A. Oesch et al. 2023) and the Complete NIRCam Grism Redshift Survey (CONGRESS-PID: 3577; PI: E. Egami; X. Lin et al. 2025a; F. Sun et al. 2025, in preparation), along with imaging data from the JWST Advanced Deep Extragalactic Survey (JADES-PID: 1181; PI: D. Eisenstein; D. J. Eisenstein et al. 2023; M. Rieke et al. 2023), to conduct a comprehensive search for broad Hα emitters at $z \approx 3.7-6.5$ in the GOODS-North field (M. Giavalisco et al. 2004). After identifying this sample of broad Hα emitters, we aim to characterize their physical properties and compare them with LRDs recently identified in other studies. The environments of these AGN and their impact on black hole growth are discussed in a companion paper (X. Lin et al. 2025c).

This paper is organized as follows: In Section 2, we provide a brief overview of the spectroscopic and imaging data utilized in this study. Section 3 details the selection process for broad Hα emitters and the methodology for 1D line fitting. In Section 4, we present and discuss the results of the 1D line fitting for our broad Hα emitters. Section 5 explores the physical properties of the broad Hα emitter sample and compares our sample with the LRD sample identified in the same field. Finally, Section 6 summarizes the main findings of this work.

Throughout this paper, we assume a flat ΛCDM cosmology with $\Omega_m = 0.3$ and $H_0 = 70\,\mathrm{km\,s^{-1}\,Mpc^{-1}}$. Magnitudes are listed in the AB system (J. B. Oke & J. E. Gunn 1983).

2. Data

2.1. Spectroscopic Data

The sample of broad Hα emitters analyzed in this paper has been selected based on spectroscopic data obtained through the JWST/NIRCam Wide Field Slitless Spectroscopy (WFSS) mode with the FRESCO and CONGRESS programs. The FRESCO survey covers 62 arcmin^2 in each of the two GOODS fields, acquiring about 2 hr deep NIRCam/grism observations using the F444W filter. These observations provide grism spectra with a resolving power of $R \sim 1600$, covering 3.8–5.0 μm for most galaxies in the field of view (FOV). CONGRESS covers the GOODS-N field only, with a footprint nearly identical to that of FRESCO. The observations with the F356W filter yield grism spectra with a resolving power of $R \approx 1400$–1610 from 3.1 to 4.0 μm. Since the GOODS-S field has grism spectroscopic coverage only in F444W, and J. Matthee et al. (2024) have already performed a systematic search for broad Hα emitters using these data, this study focuses on the GOODS-N field only. By combining the spectroscopic data from FRESCO and CONGRESS, we are able to search for broad Hα emitters within a redshift range of $z = 3.7$–6.5 in the GOODS-N field.

All the NIRCam/WFSS data were reduced using the publicly available reduction pipeline described in F. Sun et al. (2023). Here, we briefly summarize the main process. The WFSS data were first reduced to the stage 1 level by using the standard JWST stage 1 calibration pipeline `v1.11.2`. We then applied a pixel-to-pixel flat-field correction, performed 2D sky background subtraction, and assigned world coordinate system (WCS) information for each exposure. The WCS of the grism exposures was calibrated with the Gaia DR3 catalog

(Gaia Collaboration et al. 2023) by crossmatching stars identified in the simultaneously acquired NIRCam short-wavelength images with the corresponding sources in the Gaia catalog. For each source, we utilized the grism spectral tracing and dispersion models, along with the flux calibration functions presented in F. Sun et al. (2023), to extract the 2D spectra from individual grism exposures. The extracted spectra were then coadded in a common wavelength and spatial grid. Finally, we extracted the 1D spectra using optimal extraction algorithms (K. Horne 1986) and applied median filters to subtract the background and the continuum.

2.2. Multiband Imaging Data

To obtain the morphology information and estimate the physical properties of our broad Hα emitters, we utilized multiband imaging data from JADES. For the GOODS-N field, nine NIRCam images with the following filters are available: F090W, F115W, F150W, F200W, F277W, F335M, F356W, F410M, and F444W, covering a wide range of wavelengths. However, JADES covers the GOODS-N field with a different footprint compared to those of FRESCO and CONGRESS. The total overlapping area between the JADES and FRESCO/CONGRESS footprints is ~35 arcmin^2 in GOODS-N. Therefore, for about half of our broad Hα emitters, which are only covered by FRESCO and CONGRESS, imaging data are available in only six filters: F090W, F115W, F182M, F210M, F356W, and F444W. Additionally, for each broad Hα emitter, we also checked whether deep imaging data in F435W, F606W, F775W, F814W, and F850LP are available from the Hubble Space Telescope (HST)/Advanced Camera for Surveys (ACS) and HST/WFC3 (e.g., A. M. Koekemoer et al. 2011). Overall, for our broad Hα emitters with $z \approx 3.9-5.5$, these multiband imaging data provide excellent coverage of the rest-frame wavelengths from UV to optical (i.e., $<1\ \mu$m), which allows us to constrain the physical properties of these broad Hα emitters through SED fitting.

3. Broad Hα Emitter Selection

Given the large FOV of FRESCO and CONGRESS, conducting a blind search for broad Hα emitters using the grism spectra across the field is extremely time-consuming. Additionally, an extended morphology can produce a fake broad-line feature in the grism data. Therefore, to identify broad Hα emitters more efficiently, we first constructed a galaxy sample by applying compactness and photometric redshift (photo-z) criteria. Specifically, we required each source to have $\frac{F(\mathrm{F444W})r=0.''3}{F(\mathrm{F444W})r=0.''1} < 1.2$ after applying aperture correction, to ensure the selection of compact sources. To further reduce the sample size, we only included sources with photo-z values reported in JADES DR2 (F. D'Eugenio et al. 2025a) between 3 and 7, which is slightly broader than the redshift range where the Hα emission line is expected to be observable in the grism spectra from FRESCO/CONGRESS, accounting for the uncertainty in photo-z. In this way, we obtained a sample of ~600 galaxies, which is manageable for visual inspection.

Next, we conducted a visual investigation of the 1D grism spectra for each galaxy to remove contaminants that do not show a clear Hα emission line, either because no line is detected or because the observed line is inconsistent with Hα. For those potential broad Hα emitters identified by visual inspection, we fit their emission line profiles with a multi-component Gaussian profile to determine the line widths of their broad components (see Section 3.1 for more details). To select sources with broad-line features, we required our broad Hα emitters to have a broad component with a full width at half-maximum (FWHM$_{\mathrm{H}\alpha,\mathrm{broad}}$) greater than 1000 km s^{-1}. We retained only objects in which the broad component is detected with S/N $>$ 3 in line flux to ensure the broad component is real. The FWHM of the [O III] doublet was also measured when available. Below, we summarize our selection criteria:

$$\begin{aligned} \frac{F(\mathrm{F444W})r=0.''3}{F(\mathrm{F444W})r=0.''1} &< 1.2 \\ 3 < z_{\mathrm{photo}} &< 7 \\ \mathrm{S/N}_{\mathrm{H}\alpha,\mathrm{broad}} &> 3 \\ \mathrm{FWHM}_{\mathrm{H}\alpha,\mathrm{broad}} &> 1000\ \mathrm{km\ s^{-1}}. \end{aligned} \quad (1)$$

3.1. 1D Line Fitting

To determine the line widths of the broad component in these broad Hα emitters, we performed a simultaneous fit of both the narrow and broad components for Hα, and a narrow-component-only fit for [N II]$_{6549,6585}$. The line ratio of the [N II] doublet was fixed to 1:3.049, in accordance with recent results from I. Dojčinović et al. (2023). Assuming that both the narrow component of Hα and the [N II] doublet originate from the narrow-line region, we constrained their line centroids and line widths to be identical. However, as the centroid of the broad Hα component is sometimes observed to deviate slightly from that of the narrow component (e.g., J. Matthee et al. 2024), we allowed the broad and narrow components to have different line centroids by $\pm 0.01\ \mu$m (corresponding to $\approx$600–1000 km s^{-1}, depending on the redshift).

In addition to fitting the line profile using a straightforward combination of narrow and broad Gaussian components, we also tested a model incorporating Hα absorption, although previous studies suggest that detecting such absorption features requires high S/N (e.g., I. Juodžbalis et al. 2024; F. D'Eugenio et al. 2025b; X. Ji et al. 2025; V. Rusakov et al. 2025). To robustly confirm the presence of Hα absorption, we roughly followed the methodology outlined in R. Maiolino et al. (2024) and performed a Bayesian information criterion (BIC) test (A. R. Liddle 2007). For Gaussian noise, the BIC parameter is defined as

$$\mathrm{BIC} = \chi^2 + k \ln n, \quad (2)$$

where k is the number of free parameters in the model and n is the number of data points used to fit with. We required the BIC value of the fit with Hα absorption to be at least a factor of 6 larger than that of the fit without it:

$$\mathrm{BIC}_{\mathrm{No\ Absorption}} - \mathrm{BIC}_{\mathrm{Absorption}} > 6. \quad (3)$$

4. Results

4.1. 19 Broad Hα Emitters at z = 3.9–5.5

We have identified 19 broad Hα emitters in the GOODS-N field, with 10 originating from CONGRESS and nine from FRESCO. Among the 19 sources, nine are new discoveries in this work. Figure 1 shows the line fitting results for all 19 broad Hα emitters. Tables 1 and 2 summarize the basic

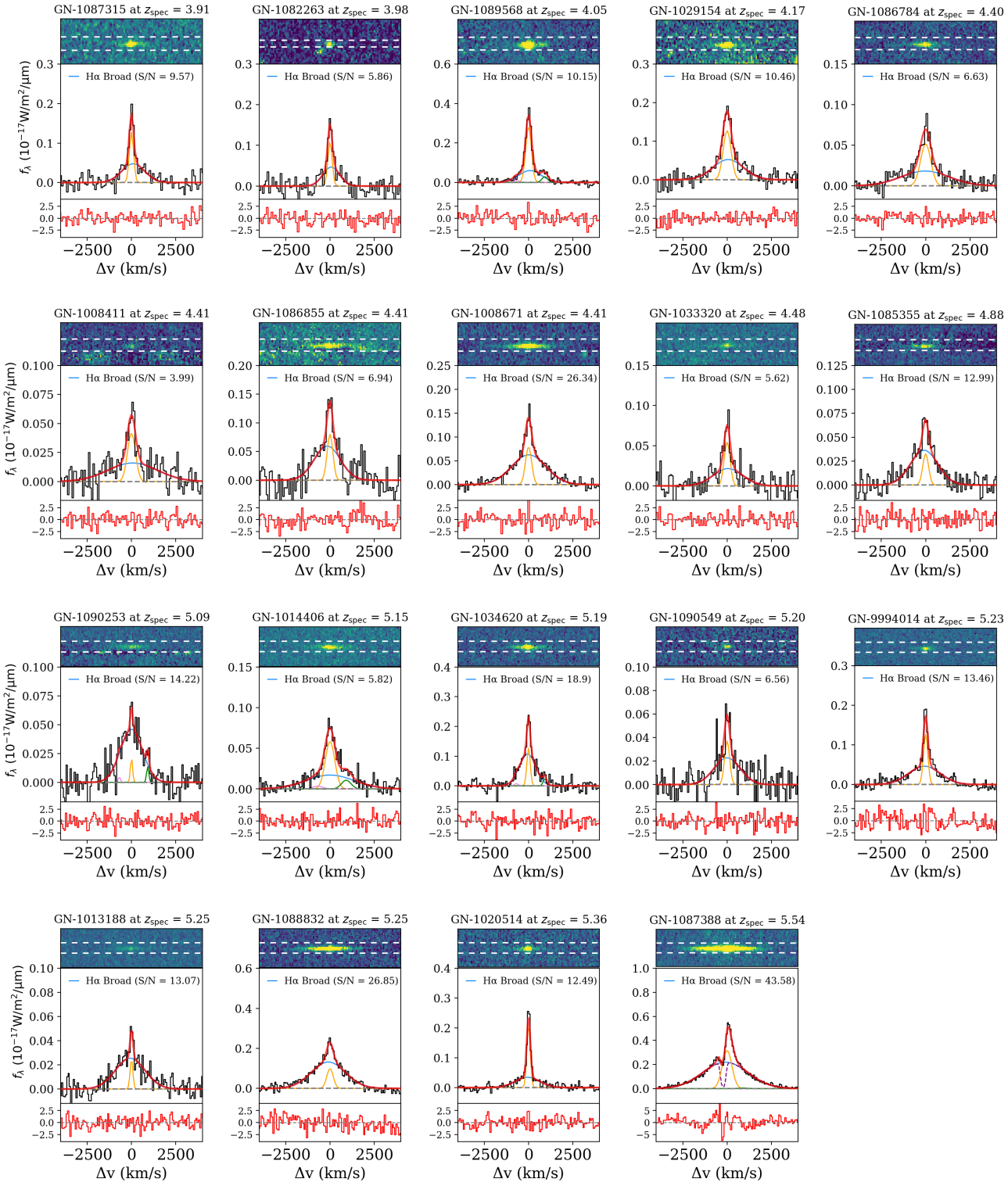

Figure 1. Multicomponent Gaussian fits to the Hα line profile for the 19 broad Hα emitters. Top subpanels: continuum-subtracted 2D spectrum. The white dashed lines represent the size of the aperture used to extract the 1D spectrum for each source. Middle subpanels: optimally extracted 1D spectrum (black), best-fit model (red), and individual components (narrow Hα: yellow; broad Hα: blue; [N II] doublet: pink and green). Bottom subpanels: residuals from the multicomponent model.

information and line fitting results for the broad Hα emitters identified in CONGRESS ($3.91 < z < 4.88$) and FRESCO ($5.09 < z < 5.54$), respectively. The reported FWHMs represent the intrinsic FWHMs of the emitters, deconvolved by the line-spread function (LSF) as described in F. Sun et al. (2025, in preparation).

Among all the broad Hα emitters, the broad Hα components exhibit an average FWHM of 2032 km s^{-1} (ranging from 1077 to 3281 km s^{-1}) and luminosity of 4.40×10^{42} erg s^{-1} (ranging from 0.9 to 32.9 $\times$ 10^{42} erg s^{-1}). [N II] emission with a S/N > 3 is detected in only two objects (i.e., GN-1034620 and GN-1089568). Hα absorption is also found to be

Table 1
Line Fitting Results for the 10 Broad Hα Emitters Identified from CONGRESS

JADES ID[a]	R.A. (deg)	Decl. (deg)	z_{spec}	$f_{H\alpha}$ (10^{-21} W m^{-2})	FWHM$_{H\alpha,broad}$ (km s^{-1})	F356W (mag)
GN-1087315[b]	189.333584	62.246178	3.91	12.5 ± 1.0	1514 ± 183	25.73
GN-1082263[b]	189.212584	62.227436	3.98	9.6 ± 1.3	1083 ± 205	24.82
GN-1089568[b]	189.151821	62.272229	4.05	23.2 ± 1.2	1462 ± 143	24.90
GN-1029154[b]	189.159025	62.260221	4.17	20.8 ± 1.5	2003 ± 225	24.96
GN-1086784	189.305706	62.236946	4.40	11.7 ± 1.2	3179 ± 504	25.42
GN-1008411[b]	189.211089	62.250271	4.41	9.4 ± 1.7	3281 ± 757	25.44
GN-1086855	189.286512	62.238138	4.41	16.9 ± 2.3	1724 ± 271	24.61
GN-1008671	189.161845	62.251054	4.41	22.1 ± 0.8	2273 ± 95	24.80
GN-1033320[b]	189.125779	62.287404	4.48	8.2 ± 1.1	1951 ± 398	25.54
GN-1085355[b]	189.094365	62.198974	4.88	10.7 ± 0.8	1801 ± 158	25.42

Notes.
[a] IDs are from JADES DR2 (F. D'Eugenio et al. 2025a).
[b] New broad Hα emitters identified in this work. The other emitters are already reported by A. Covelo-Paz et al. (2025).

Table 2
Line Fitting Results for the Nine Broad Hα Emitters Identified from FRESCO

JADES ID[a]	R.A. (deg)	Decl. (deg)	z_{spec}	$f_{H\alpha}$ (10^{-21} W m^{-2})	FWHM$_{H\alpha,broad}$ (km s^{-1})	$f_{[O\ III]\lambda5007}$ (10^{-21} W m^{-2})	FWHM$_{[O\ III]}$ (km s^{-1})	F444W (mag)
GN-1090253	189.285544	62.280781	5.09	10.0 ± 0.7	1455 ± 105	⋯	⋯	24.65
GN-1014406	189.072090	62.273431	5.15	13.2 ± 1.5	3212 ± 639	⋯	⋯	25.44
GN-1034620[b]	189.159764	62.295924	5.19	21.1 ± 1.1	1077 ± 71	⋯	⋯	24.31
GN-1090549[b]	189.235941	62.285544	5.20	7.5 ± 1.0	1721 ± 307	⋯	⋯	25.92
GN-9994014	189.300125	62.212044	5.23	19.5 ± 1.1	2084 ± 156	⋯	⋯	24.92
GN-1013188	189.057100	62.268940	5.25	8.0 ± 0.6	1957 ± 147	⋯	⋯	25.38
GN-1088832	189.344282	62.263368	5.25	49.7 ± 1.8	2256 ± 91	8.8 ± 0.6	243 ± 24	23.67
GN-1020514	189.179302	62.292533	5.36	15.5 ± 0.7	1612 ± 140	19.5 ± 0.4	197 ± 7	24.79
GN-1087388	189.281014	62.247308	5.54	130.1 ± 2.7	2965 ± 55	3.5 ± 0.3	150 ± 23	22.93

Notes.
[a] IDs are from JADES DR2 (F. D'Eugenio et al. 2025a).
[b] New broad Hα emitters identified in this work. The other emitters are already reported by J. Matthee et al. (2024).

rare within our sample, with a robust detection observed in only one object (i.e., GN-1087388), consistent with J. Matthee et al. (2024), who also reported the presence of an absorption feature in this source. However, we cannot assess the presence of Hα absorption with grism data. As noted earlier, recent studies with NIRSpec have shown that detecting such absorption features typically requires high S/N or higher resolution (e.g., I. Juodžbalis et al. 2024; F. D'Eugenio et al. 2025b; X. Ji et al. 2025; V. Rusakov et al. 2025). Given the relatively low S/N of many sources in our sample, it remains possible that Hα absorption is present but remains undetected in some cases.

Although the line centroids of the broad and narrow components are allowed to be different, the majority of objects exhibit offsets of <100 km s^{-1}, with the largest offset of 150 km s^{-1} observed in GN-1086855. We find that the broad components contribute, on average, about 72% of the total Hα luminosity, with only one object exhibiting a broad component contribution of less than 50%. We note that our sample exhibits a higher average contribution from the broad component compared to that of the Type 1 AGN identified with NIRSpec in JADES (i.e., 46% ± 25%; I. Juodžbalis et al. 2025). This difference is likely due to the lower S/N of our sample, which may hinder the detection of faint broad components. However, by taking the uncertainties into consideration, our average broad-component contribution remains consistent with that of I. Juodžbalis et al. (2025) at the 1σ level.

Figure 2 presents false-color stamp images of the 19 discovered broad Hα emitters while Figure 3 illustrates the sky positions of these emitters, overlaid with the footprints of CONGRESS, FRESCO, and JADES. Notably, our sample includes seven broad Hα emitters from FRESCO, as reported by J. Matthee et al. (2024), and three broad Hα emitters from CONGRESS, as reported by A. Covelo-Paz et al. (2025). We note that two broad Hα emitters in A. Covelo-Paz et al. (2025) were excluded as they do not meet our selection criteria. A detailed explanation is provided in Appendix A.

We highlight nine broad Hα emitters newly identified in this work in Tables 1 and 2. The exact reasons for their absence in previous studies remain unclear. For the seven CONGRESS sources not reported in A. Covelo-Paz et al. (2025), the paper does not provide enough information to make an assessment. Regarding the two FRESCO sources not reported in J. Matthee et al. (2024), we suspect that GN-1090549 may have been excluded due to its relatively low S/N, as J. Matthee et al. (2024) adopted a stricter cut (S/N > 5) than we did. Although GN-1090549 shows a broad component with S/N > 5 in our analysis, differences in 1D grism spectrum extraction methods between the two studies may explain this discrepancy. For GN-1034620, we note that this source overlaps with a giant

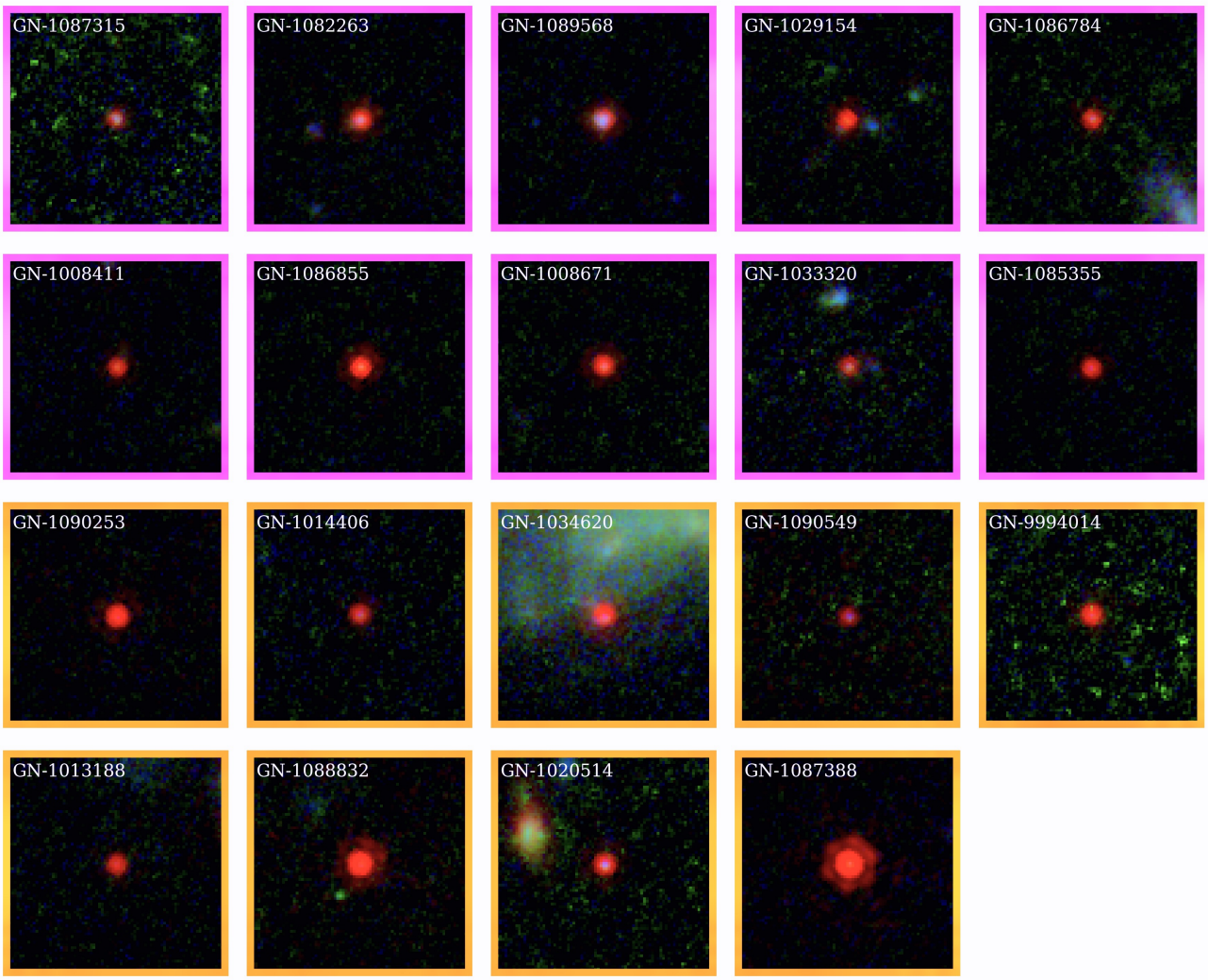

Figure 2. False-color stamps of the 19 broad Hα emitters identified in this work. Emitters detected in FRESCO are marked in orange and the stamps are constructed using NIRCam F115W+F210M+F444W imaging data, while those detected in CONGRESS are marked in violet and the stamps are constructed using NIRCam F115W+F210M+F356W imaging data. Each stamp spans 2.″5 × 2.″5 × 2.5 arcsec^2.

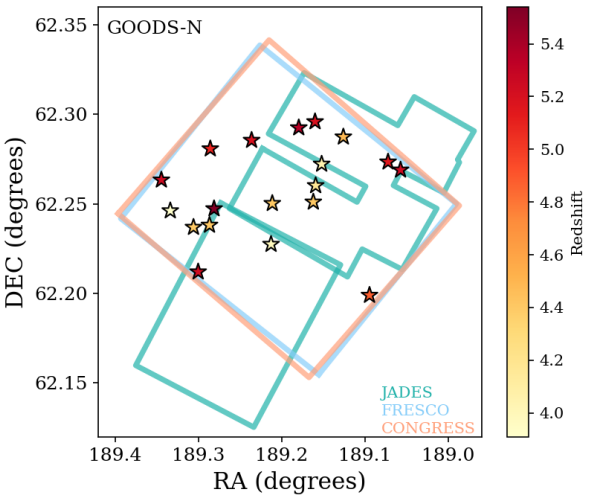

Figure 3. Sky positions of the 19 broad Hα emitters (stars) discovered in the GOODS-N field, color-coded by redshift. The JADES, FRESCO, and CONGRESS footprints are overlaid with light green, blue, and red lines, respectively.

local galaxy, and it is possible that segmentation differences led to its being excluded from their sample.

4.2. Narrow [O III] Lines and AGN Origin of the Broad Hα Lines

Since the JWST/NIRCam grism spectra in our study only cover two wideband filters (i.e., F356W and F444W), the [O III] doublet is within the wavelength coverage for only three emitters in our sample. Figure 4 shows the 1D line fitting results for these three sources. Since the FWHM observed in [O III] is significantly smaller than that observed in Hα, this effectively rules out the possibility that the broad components originate from galactic outflows.

For emitters without [O III] coverage, although we cannot entirely exclude the possibility of galactic outflows, the majority exhibit broad-component FWHM values significantly larger than 1000 km s^{-1}, along with broad-to-narrow Hα flux ratios exceeding 50%. In contrast, broad components associated with galactic outflows typically exhibit narrower FWHMs, ranging from a few hundred to ∼1000 km s^{-1}, depending on whether the outflows are driven by star

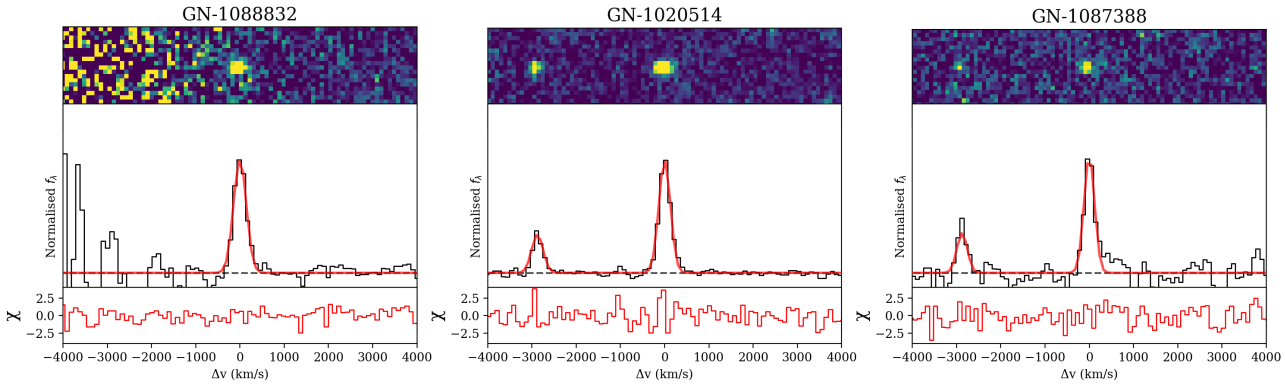

Figure 4. Single-component Gaussian fits (red) to the observed [O III] line profiles (black) of three broad Hα line emitters. Top subpanels: continuum-subtracted 2D spectrum. Bottom subpanels: residuals from the single-component Gaussian model. Line fitting results are summarized in Table 2.

formation or AGN activity, and show broad-to-narrow Hα flux ratios of ∼50% (see J. Matthee et al. 2024 and references therein). We also note that in published NIRSpec studies, nearly all broad Hα emitters show narrow [O III] emission, with their broad Balmer lines consistently attributed to the AGN broad-line region (BLR; e.g., Y. Harikane et al. 2023; J. E. Greene et al. 2024). Therefore, it is reasonable to assume that the broad components in our sample are primarily caused by AGN activity.

5. Discussion

5.1. Luminosity Function of Broad-line Hα Emitters

We compute the broad Hα luminosity function (LF) for the 19 broad Hα emitters identified in this work. The broad Hα LF is computed following the direct $1/V_{\rm max}$ method (M. Schmidt 1968):

$$\Phi(L) = \frac{1}{d\log L}\sum_i \frac{1}{C_i V_{{\rm max},i}} \quad (4)$$

where L is the broad Hα luminosity of each LF bin, and C_i and $V_{{\rm max},i}$ represent the completeness correction and the maximum survey volume for the ith broad Hα emitter, respectively. The completeness correction and maximum survey volume are measured following the methodology described in X. Lin et al. (2024). The uncertainties in the LF are estimated via Monte Carlo experiments. Table 3 summarizes the broad Hα LFs measured in this work.

We present the derived broad Hα LFs of our sample in Figure 5. For comparison, we also include the broad Hα LFs derived from JWST-selected broad-line AGN in other studies (X. Lin et al. 2024, 2026; J. Matthee et al. 2024), as well as the quasar broad Hα LF at $z \sim 5$, obtained by converting the bolometric LFs from X. Shen et al. (2020). The conversion assumes the empirical relations between the bolometric luminosity and the AGN-induced Hα luminosity from J. E. Greene & L. C. Ho (2005), with the bolometric correction from G. T. Richards et al. (2006). We find that at the faint end (i.e., $L_{{\rm H}\alpha,{\rm broad}} < 10^{43}$ erg s^{-1}), the number density of broad Hα emitters is significantly higher than the extrapolation of the quasar LF. At the bright end, however, the LF begins to converge toward that of quasars. This trend is consistent with LFs derived from other JWST-selected AGN in the literature, suggesting a prevalence of broad-line AGN in the early Universe.

Table 3
Broad Hα LFs of Our Broad Hα Emitter Sample

$\log L_{{\rm H}\alpha,{\rm broad}}$	$\Delta \log L_{{\rm H}\alpha,{\rm broad}}$	N	Φ (10^{-5} Mpc^{-3} dex^{-1})
42.117	0.414	7	$4.891^{+2.634}_{-2.362}$
42.531	0.414	10	$6.312^{+1.963}_{-3.523}$
43.153	0.819	2	$1.080^{+2.483}_{-0.893}$

5.2. The L_{bol}–M_{BH} Relation

To gain insights into the accretion efficiency and growth rates of our broad Hα emitters, we estimate the black hole mass ($M_{\rm BH}$) and AGN bolometric luminosity ($L_{\rm bol}$) of our broad Hα emitters following the methodology widely adopted in recent studies (e.g., Y. Harikane et al. 2023; D. D. Kocevski et al. 2023; H. Übler et al. 2023; J. Matthee et al. 2024). More specifically, the $M_{\rm BH}$ are estimated using the virial relation proposed by A. E. Reines et al. (2013),

$$\begin{aligned}\log_{10}(M_{\rm BH}/M_\odot) = 6.57 &+ \log_{10}(\epsilon) \\ &+ 0.47\log_{10}(L_{{\rm H}\alpha,{\rm broad}}/10^{42}\ {\rm erg\ s^{-1}}) \\ &+ 2.06\ \log_{10}({\rm FWHM_{broad}}/10^3\ {\rm km\ s^{-1}}),\end{aligned} \quad (5)$$

where ϵ represents the scale factor, which we assume to be 1.075, consistent with the value adopted in A. E. Reines & M. Volonteri (2015).

Regarding AGN bolometric luminosity, we follow the approach described in Y. Harikane et al. (2023), estimating it from the luminosity of the broad Hα component (J. E. Greene & L. C. Ho 2005) and applying the corresponding bolometric correction from G. T. Richards et al. (2006):

$$\begin{aligned}L_{\rm bol}/10^{44}\ {\rm erg\ s^{-1}} &= 10.33 \\ &\times (L_{{\rm H}\alpha,{\rm broad}}/5.25\times 10^{42}\ {\rm erg\ s^{-1}})^{0.864}.\end{aligned} \quad (6)$$

Table 4 presents the estimated values of $M_{\rm BH}$ and $L_{\rm bol}$ for all the broad Hα emitters identified in this work. The associated uncertainties are calculated using error propagation.

We plot the $M_{\rm BH}$ versus the Hα-inferred AGN bolometric luminosities in Figure 6. For comparison, we include UV-selected luminous quasars at $z > 6.3$ from J. Yang et al. (2021), broad-line AGN (BLAGN) identified with NIRSpec

Table 4
Physical Properties of the Broad Hα Emitters

JADES ID	$L_{\mathrm{H}\alpha,\mathrm{broad}}$ (10^{42} erg s^{-1})	$\log(M_{\mathrm{BH}}/M_{\odot})$	L_{bol} (10^{44} erg s^{-1})	$L_{\mathrm{H}\alpha,\mathrm{broad}}/L_{\mathrm{H}\alpha,\mathrm{tot}}$	$\log(M_{*}/M_{\odot})$
GN-1014406	2.21 ± 0.38	7.81 ± 0.18	4.88 ± 0.73	0.60 ± 0.05	9.30 ± 0.42
GN-1085355	2.22 ± 0.17	7.29 ± 0.08	4.91 ± 0.33	0.84 ± 0.04	8.33 ± 0.35
GN-1087388	32.90 ± 0.76	8.29 ± 0.02	50.50 ± 1.00	0.76 ± 0.01	10.87 ± 0.26
GN-1088832	12.70 ± 0.47	7.85 ± 0.04	22.20 ± 0.71	0.88 ± 0.01	9.64 ± 0.21
GN-1008671	3.49 ± 0.13	7.59 ± 0.04	7.26 ± 0.24	0.81 ± 0.01	10.14 ± 0.46
GN-1013188	2.14 ± 0.16	7.36 ± 0.07	4.75 ± 0.31	0.92 ± 0.02	9.18 ± 0.23
GN-1020514	2.54 ± 0.20	7.22 ± 0.08	5.52 ± 0.38	0.53 ± 0.02	10.14 ± 0.42
GN-1029154	2.16 ± 0.21	7.38 ± 0.10	4.79 ± 0.39	0.61 ± 0.04	8.12 ± 0.32
GN-1033320	1.09 ± 0.19	7.22 ± 0.19	2.65 ± 0.41	0.66 ± 0.06	9.76 ± 0.38
GN-1034620	4.83 ± 0.26	6.99 ± 0.06	9.62 ± 0.44	0.81 ± 0.02	10.15 ± 0.38
GN-1082263	0.91 ± 0.16	6.65 ± 0.17	2.28 ± 0.33	0.63 ± 0.07	8.77 ± 0.40
GN-1086784	1.41 ± 0.21	7.71 ± 0.15	3.31 ± 0.43	0.62 ± 0.04	8.38 ± 0.29
GN-1086855	2.52 ± 0.36	7.28 ± 0.14	5.48 ± 0.69	0.77 ± 0.06	8.85 ± 0.43
GN-1087315	1.22 ± 0.13	7.01 ± 0.11	2.92 ± 0.26	0.67 ± 0.04	8.76 ± 0.28
GN-1089568	1.66 ± 0.16	7.04 ± 0.09	3.83 ± 0.32	0.45 ± 0.03	8.76 ± 0.25
GN-1090253	2.60 ± 0.18	7.13 ± 0.07	5.63 ± 0.34	0.96 ± 0.02	9.31 ± 0.50
GN-1090549	1.62 ± 0.25	7.19 ± 0.16	3.75 ± 0.49	0.76 ± 0.06	9.09 ± 0.19
GN-1008411	1.28 ± 0.32	7.72 ± 0.21	3.06 ± 0.66	0.70 ± 0.06	8.66 ± 0.64
GN-9994014	4.08 ± 0.30	7.55 ± 0.07	8.31 ± 0.54	0.72 ± 0.02	10.50 ± 0.24

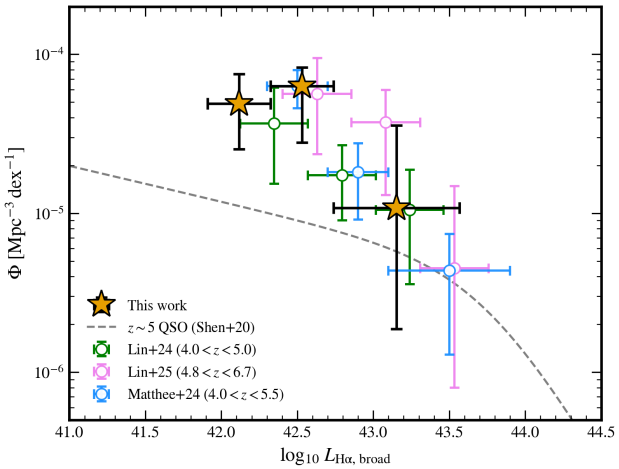

Figure 5. The broad Hα LFs derived from the broad Hα emitter sample identified in this work (yellow stars). For comparison, the broad Hα LFs measured in J. Matthee et al. (2024), X. Lin et al. (2024), and X. Lin et al. (2026) are also shown. The gray dashed curve denotes the extrapolation of the quasar bolometric LF at $z \sim 5$ from X. Shen et al. (2020), converted to broad Hα luminosity using the local relation between the quasar bolometric and broad-line Hα luminosities.

grating spectroscopy at $z \approx 4.4-6.8$ from R. Maiolino et al. (2024),[16] BLAGN at $z \approx 4-7$ from Y. Harikane et al. (2023), and BLAGN detected with NIRSpec prism spectroscopy at $z \approx 4.5-7$ from J. E. Greene et al. (2024). Notably, the M_{BH} for those BLAGN were derived using the same methodology employed in this study, whereas J. Yang et al. (2021) estimated M_{BH} based on the continuum luminosity at 3000 Å and the FWHM of the Mg II line.

The majority of our sample is found to be accreting at an Eddington ratio of the order of 0.1, lower than that of UV-selected luminous quasars, consistent with the intrinsically faint nature of our broad Hα emitters. These moderate accretion rates are in line with those reported for BLAGN in R. Maiolino et al. (2024) and J. E. Greene et al. (2024). In contrast, the bolometric luminosities of the BLAGN in Y. Harikane et al. (2023) are derived using a more complex methodology, where L_{bol} as estimated from Equation (6) is treated as a lower limit. Taking this into account, we find no significant difference in the inferred accretion rates between our sample and that of Y. Harikane et al. (2023).

Interestingly, we notice that the BLAGN identified with NIRSpec prism ($R \sim 100$) spectroscopy in J. E. Greene et al. (2024) tend to occupy the high-mass end of the M_{BH} distribution relative to our sample. The recent JWST Cycle 3 General Observer program Slitless Areal Pure-parallel High-redshift Emission Survey (SAPPHIRES-PID: 6434; PI: E. Egami; F. Sun et al. 2025) observed one BLAGN (FWHM ~ 4000 km s^{-1}) from J. E. Greene et al. (2024) with the F444W grism, providing an independent Hα line measurement. While the source still exhibits a broad feature, the line width appears significantly narrower (FWHM ~ 1300 km s^{-1}). Given the grism's higher spectral resolution, we adopt the latter measurement and mark the resulting L_{bol} and M_{BH} with an "X" in Figure 6, which suggests the possibility that some of the line widths measured by NIRSpec/prism may be overestimated. The details of the analysis of the SAPPHIRES spectrum are presented in Appendix B.

5.3. The M_{BH}–M_{*} Relation

In this work, the stellar masses (M_{*}) of the AGN hosts are measured by SED fitting using the `Prospector` Bayesian inference framework (J. Leja et al. 2017; B. D. Johnson et al. 2021; B. Johnson et al. 2022) based on the Flexible Stellar Population Synthesis (C. Conroy et al. 2009; C. Conroy & J. E. Gunn 2010) code. To achieve reliable AGN identification, we adopt a modified version of `Prospector` presented in J. Lyu et al. (2024), which incorporates a semiempirical model for AGN UV-to-mid-infrared continua with nebular emission lines and dust attenuation and replaces the default AGN torus model in `Prospector`.

During the SED fitting process, we include not only the deep JWST/NIRCam photometry but also multiband data spanning

[16] We exclude three sources from R. Maiolino et al. (2024) that exhibit two broad components.

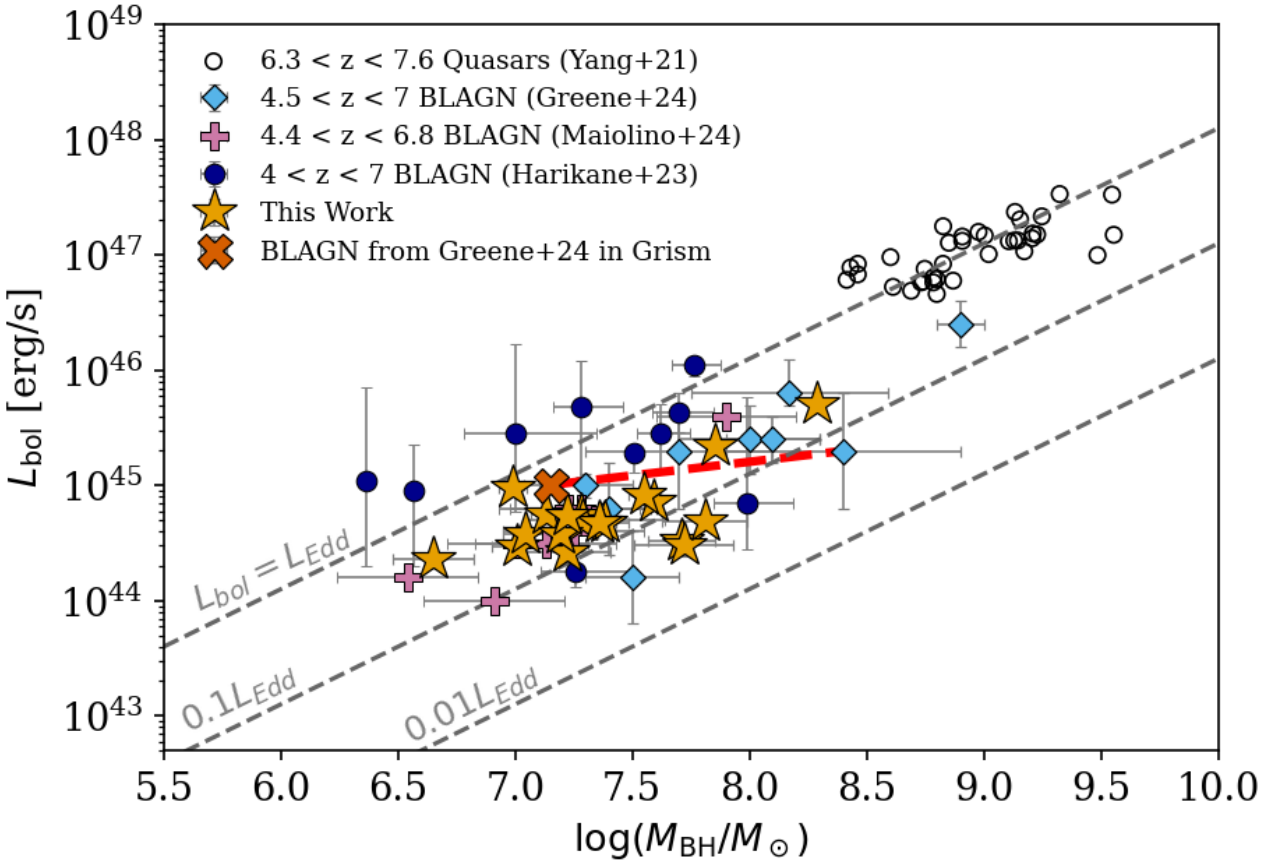

Figure 6. Distribution of 19 broad Hα line emitters (yellow stars) on the AGN L_{bol}–M_{BH} plane. For comparison, we include BLAGN identified in other studies: R. Maiolino et al. (2024) (violet pluses), Y. Harikane et al. (2023) (dark blue dots), and J. E. Greene et al. (2024) (blue diamonds). We also include UV-selected bright quasars from J. Yang et al. (2021) (empty black circles). One of the NIRSpec/prism-detected BLAGN in J. E. Greene et al. (2024) (FWHM $\sim$ 4000 km s^{-1}) was also observed with NIRCam/grism (SAPPHIRES), but the latter shows a much narrower line width ($\sim$1300 km s^{-1}; see Appendix B); its grism-based AGN L_{bol} and M_{BH} are represented by the orange "X" marker, with the dashed red line indicating how the position shifts between the grism- and prism-based values. The dashed gray lines represent $L_{bol} = L_{Edd}$, $L_{bol} = 0.1L_{Edd}$, and $L_{bol} = 0.01L_{Edd}$.

the optical to near-infrared from HST/ACS and HST/WFC3, as well as longer-wavelength infrared data from Spitzer, if they are available. Examples of galaxy SED fitting results are shown in Figure 7. The bottom panel presents the only source with a robust detection at longer wavelengths from Spitzer. For the remaining sources, due to the limited wavelength coverage of the NIRCam photometry, clear AGN signatures are identified through SED analysis in only nine out of 18 galaxies, despite the presence of broad Hα emission lines. Therefore, follow-up MIRI observations to obtain mid-infrared data for these broad Hα emitters would be valuable for better constraining their physical properties. Table 4 lists the best-fit values and corresponding uncertainties of M_* for all broad Hα emitters. Table 4 also summarizes the key physical properties of the 19 broad Hα emitters.

Figure 8 illustrates the distribution of the broad Hα emitters identified in this study on the M_{BH}–M_* plane. To further explore the evolution of the M_{BH}–M_* relation over cosmic time, we incorporate AGN recently discovered with JWST across a wide redshift range. These include one potential AGN at $z > 10$, UHZ 1 (Á. Bogdán et al. 2024), as well as BLAGN in the GOODS-N field at $4.4 < z < 6.8$ (R. Maiolino et al. 2024) and $1 < z < 4$ (Y. Sun et al. 2025a), and BLAGN at $4 < z < 7$ identified by Y. Harikane et al. (2023). The local M_{BH}–M_* relations for AGN hosts derived in A. E. Reines & M. Volonteri (2015) (hereafter RV15) and J. E. Greene et al. (2020) (all, limits case; hereafter GSH20) are also included for comparison purposes.

We find that nearly all AGN recently revealed by JWST observations at $z > 4$ lie above RV15, with the majority located significantly above the relation. When compared to the GSH20 relation, which is considered a more robust local relation that shows no bias with galaxy type and provides a better match to broad-line-selected AGN at $1 < z < 4$ (Y. Sun et al. 2025b), the offset is somewhat reduced. Nevertheless, many sources still exhibit higher M_{BH}/M_* ratios than those predicted by GSH20. The overmassive M_{BH} relative to the M_* of the host galaxy, when compared with the local scaling relations, is consistent with findings from numerous previous studies of AGN at similar redshifts (e.g., D. D. Kocevski et al. 2023; H. Übler et al. 2023). These results may suggest a different evolution path of the M_{BH}–M_* relation in the early Universe compared to that observed locally. Additionally, the presence of SMBHs with M_{BH} above the local scaling relations aligns with theoretical predictions from models invoking heavy black hole seeds and super-Eddington accretion, which are proposed to explain the rapid growth of SMBHs at very early time (A. Trinca et al. 2022; R. Schneider et al. 2023; M. Volonteri et al. 2023). Alternatively, the growth of the host galaxy can also be suppressed by strong feedback processes (see Y. Zhu et al. 2025 and references therein). However, it is also important to note that, although our AGN

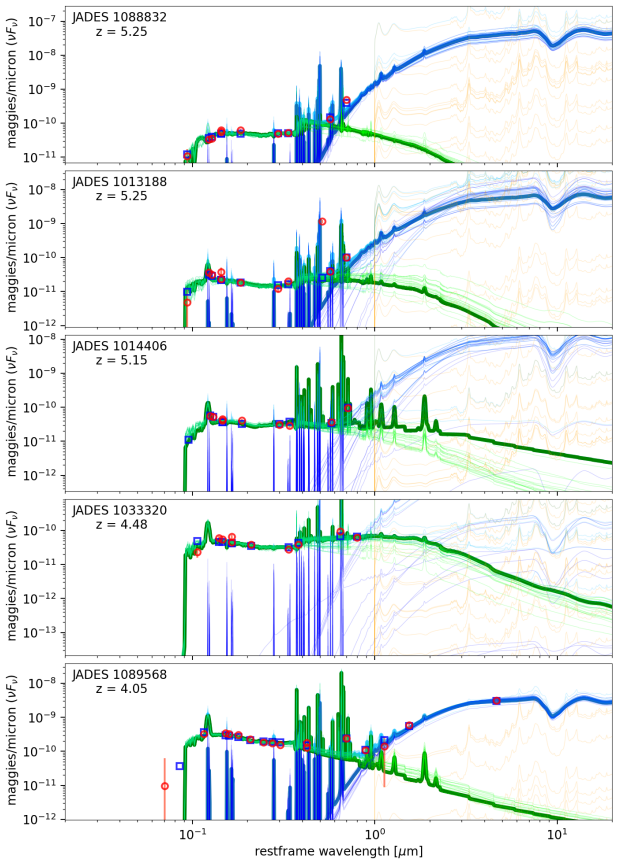

Figure 7. Example SED fittings of our sample: the green line is the stellar component, the blue line is the AGN model, and the orange line is the galaxy dust emission. The measurements are shown as open red circles with error bars, and the blue squares are the result of synthetic photometry on the model. The thin lines are showing 20 randomly selected models from the posterior.

sample is selected based on the presence of broad emission lines in spectroscopy, selection bias still exists to some extent. Specifically, due to the detection limits of the grism observations and the requirement of FWHM > 1000 km s^{-1}, we may fail to detect very faint, low-mass AGN (see Section 5.6 for more details), which could otherwise help fill the observed gap between our sample and the local $M_{\rm BH}$–M_* relation.

5.4. Are Broad-line Emitters LRDs?

In this section, we evaluate the fraction of our spectroscopically confirmed broad Hα emitters that can be photometrically classified as LRDs by applying the selection criteria outlined in P. Rinaldi et al. (2025a):

1. Blue slope: F150W $-$ F200W < 0.8 mag
2. Red slope: F277W $-$ F444W > 0.7 mag

Since the compactness criterion is already applied during the selection of broad Hα emitters, and the possibility of these sources being brown dwarfs is excluded, we only implement color cuts for our sample. Of the 19 sources in our sample, only nine are covered by JADES imaging, and thus have available photometry in the F150W, F200W, and F277W bands. For the remaining 10 sources, we use `Synphot` to estimate their photometry in these bands based on their best-fit SEDs.

The left panel of Figure 9 shows the positions of the broad Hα emitters on the color–color plot. We find that a significant fraction of our sample ($\sim$42%) cannot be photometrically selected as LRDs, with the majority (seven out of eight) failing to meet the red slope criterion. This result is consistent with K. N. Hainline et al. (2025), who applied a stricter red slope threshold and found that only 30% of spectroscopically identified BLAGN with JWST meet the LRD selection criteria. These findings suggest that not all broad-line emitters with a compact, red appearance exhibit the characteristic "V-shaped" SED of LRDs, and that many lack a steep red slope.

Additionally, since bright Hα emission is observed in F444W for all broad Hα emitters identified in FRESCO, applying a relatively loose red slope criterion raises concerns about those sources that satisfy the LRD color selection. It remains unclear whether these sources intrinsically exhibit such steep red slopes, or whether their observed colors are primarily driven by line-boosting effects (K. N. Hainline et al. 2025).

A more conservative approach to selecting LRDs with a high AGN yield through color cuts involves applying a higher cut on the red slope, in order to reduce contamination from line-boosting effects, as proposed by G. Barro et al. (2024) and J. E. Greene et al. (2024). In the left panel of Figure 9, we add the selection criteria proposed in both studies:

1. Red slope: F277W $-$ F444W > 1.5 mag (G. Barro et al. 2024)
2. Red slope: F277W $-$ F444W > 1.6 mag (J. E. Greene et al. 2024)

However, even without considering the blue slope requirement, applying these stricter thresholds yields only three LRD candidates in both cases, missing eight LRDs identified by our original selection criteria and 84% of our broad-line emitters. Therefore, the trade-off between completeness and purity in color-based LRD selection should be taken into consideration when determining the appropriate color cuts to apply.

In addition to color-based selection, D. D. Kocevski et al. (2025) proposed an alternative approach for identifying LRDs by applying cuts on the UV and optical continuum slopes, derived from fitting photometry across multiple bands blueward and redward of the Balmer break at 3645 Å. This method enables the detection of LRDs with reduced contamination from galaxies that exhibit strong Balmer breaks but lack a rising red continuum. To make optimal use of the available photometry, we derive the UV continuum slope using the F090W, F115W, and F182M bands. For sources at redshift $z < 4.75$, we use F210M, F277W, and F356W to measure the optical continuum slope, while for higher-redshift sources (i.e., $z \geqslant 4.75$), we instead use F277W, F356W, and F444W. For sources lacking photometry in F277W, we estimate their fluxes in F277W from their best-fit SEDs. The uncertainties on the measured slopes are estimated using a Monte Carlo approach following the methodology described in D. D. Kocevski et al. (2025).

We adopt the same cuts used in D. D. Kocevski et al. (2025):

1. Blue slope: $\beta_{\rm UV} < -0.37$
2. Red slope: $\beta_{\rm opt} > 0$

The right panel of Figure 9 shows the distribution of our sample in the $\beta_{\rm opt}$–$\beta_{\rm UV}$ plane. Based on this selection approach, 47% of our sample do not satisfy the selection criteria. Similarly, most of the outliers fail to satisfy the red slope criterion. All three LRD selection techniques miss an

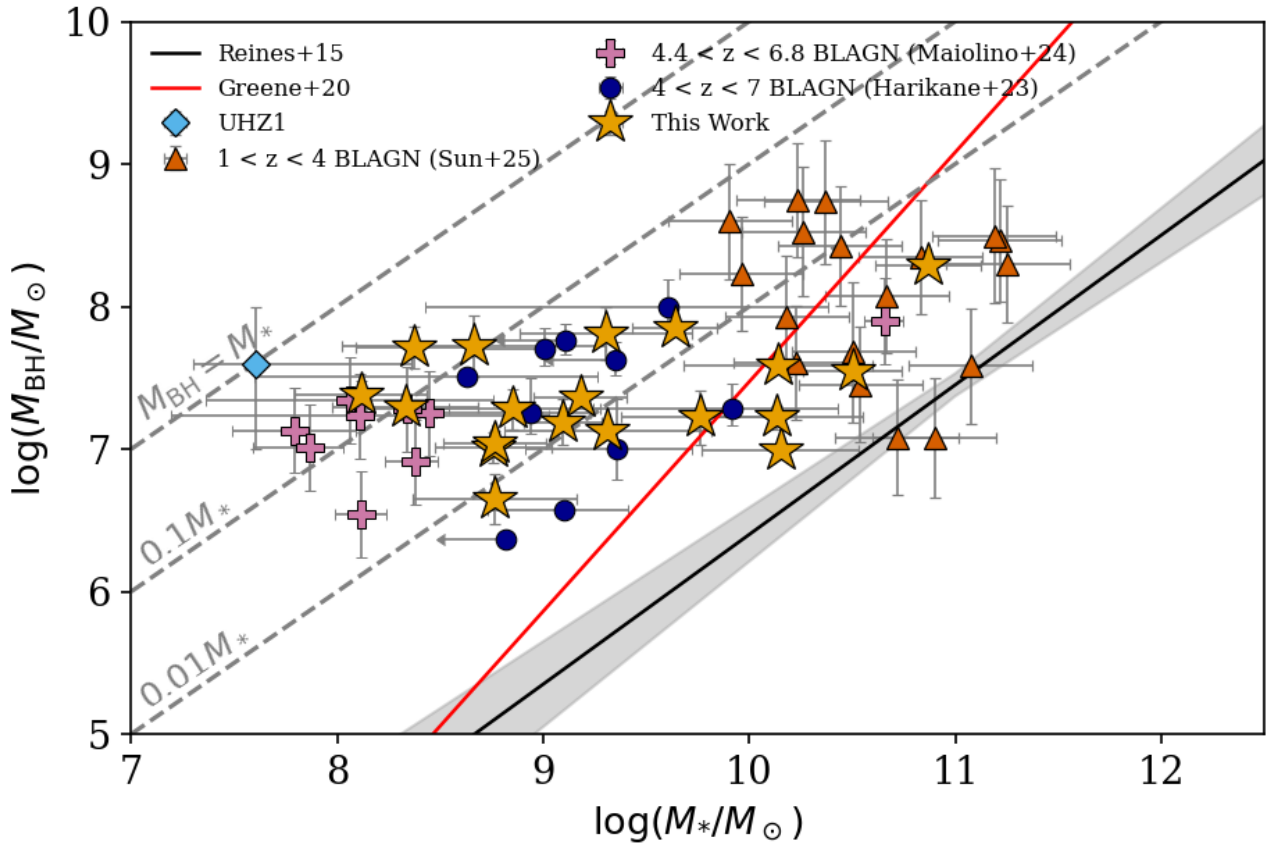

Figure 8. M_{BH}–M_* relation for the broad Hα emitter sample (yellow stars). For comparison, we include BLAGN samples spanning a wide redshift range from the literature: R. Maiolino et al. (2024) (violet pluses), Y. Harikane et al. (2023) (dark blue dots), and Y. Sun et al. (2025a) (red triangles). One potential $z > 10$ AGN, UHZ 1 (blue diamond), is also shown. The solid black line and shaded gray region represent the local M_{BH}–M_* relation derived by A. E. Reines & M. Volonteri (2015), while the solid red line shows the local relation (all, limits case) from J. E. Greene et al. (2020).

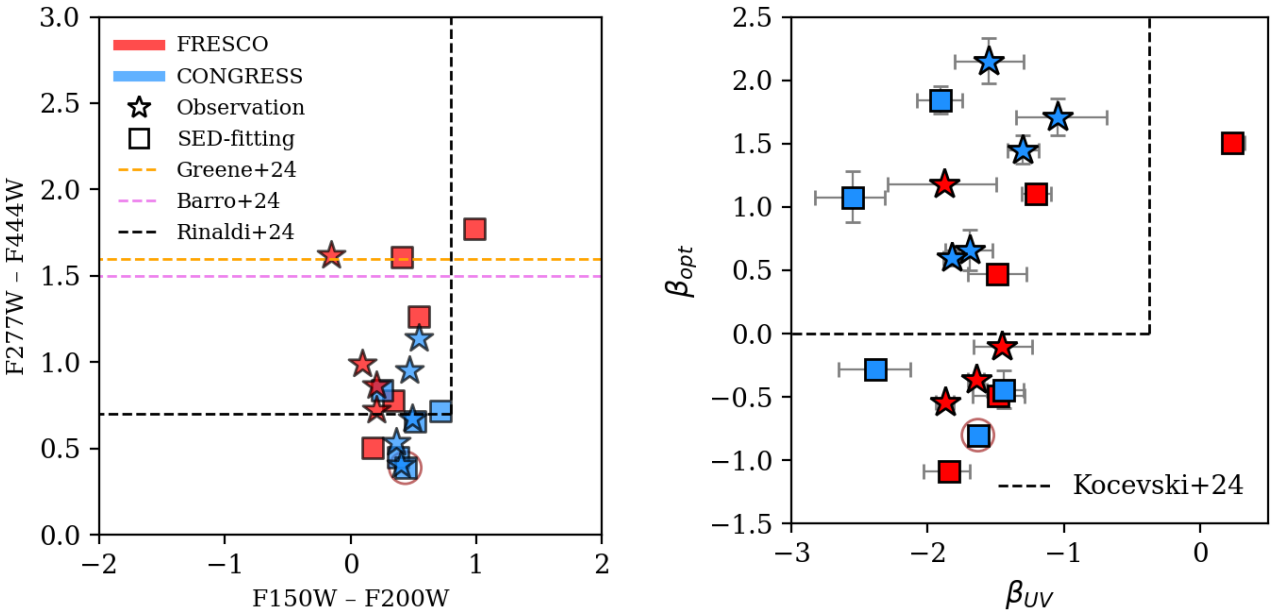

Figure 9. Left panel: distribution of broad Hα emitters on the color–color diagram (red: FRESCO; blue: CONGRESS). Stars indicate sources with available photometric measurements in the F150W, F200W, and F277W bands, while squares represent sources for which photometry in these bands is estimated from best-fit SEDs. The dashed black lines indicate the LRD selection criteria defined by P. Rinaldi et al. (2025a), while the dashed orange and violet lines represent LRD selection criteria proposed by J. E. Greene et al. (2024) and G. Barro et al. (2024), respectively, which have shown high-yield selections of AGN. Right panel: distribution of our sample in the β_{opt}–β_{UV} plane. The dashed black lines indicate the LRD selection criteria adopted in D. D. Kocevski et al. (2025). The brown circle in each panel highlights the broad Hα emitter with mid-infrared detections from Spitzer.

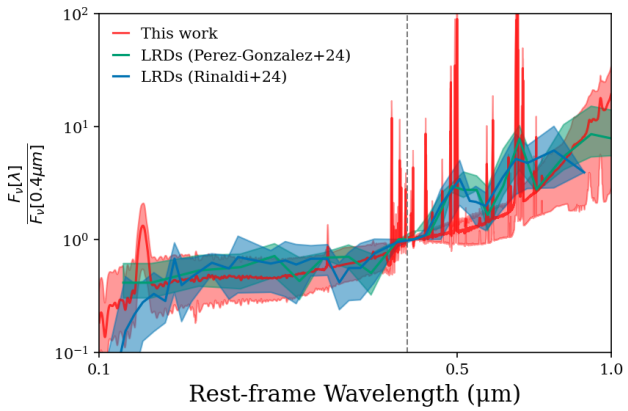

Figure 10. Stacked SEDs for the broad-line emitter sample identified in this work (red) and for the LRD samples selected in P. Rinaldi et al. (2025a) (dark blue) and P. G. Pérez-González et al. (2024) (teal green), normalized at a rest-frame wavelength of 0.4 μm. Shaded regions denote the 1σ uncertainties on the average SEDs.

important fraction of our broad-line emitters (i.e., 42%, 84%, and 47%) suggesting that current LRD selection methods may overlook a substantial fraction of the broad-line emitter population.

However, most of the broad Hα emitters that fail the LRD color selection do not satisfy the red slope criterion, with the majority originating from CONGRESS. In these cases, the [O III] doublet falls within the F277W filter, making the F277W − F444W color less red, and causing these sources to fall outside the selection boundary. An example of an object that clearly exhibits LRD-like behavior in its SED but is not color-selected as an LRD due to strong [O III] emission is presented in P. Rinaldi et al. (2025b). This further highlights the challenges and limitations of color-based LRD selection at these redshifts.

While several alternative color selection criteria of LRDs have been proposed in the literature (e.g., J. E. Greene et al. 2024; P. G. Pérez-González et al. 2024), we adopt the criteria used by P. Rinaldi et al. (2025a) in this work to maintain consistency, as their LRD sample is also constructed in the GOODS-N field.

To further explore the relationship between broad-line emitters and photometrically selected LRDs, we perform a comparison between the average SEDs of our broad Hα emitters and the LRD sample selected in P. Rinaldi et al. (2025a). We follow the methodology outlined in P. G. Pérez-González et al. (2024) to derive the average SED of the LRD sample by stacking the SEDs of LRDs with available spectroscopic redshifts (including their emission lines) and computing the mean flux for every 10 consecutive data points in the wavelength-ordered list. In contrast, the average SED of our broad Hα emitter sample is constructed using the best-fit SEDs obtained in Section 5.3, as about half of the sources in our sample have photometry available in only six filters. Figure 10 displays the average rest-frame SEDs for both broad Hα emitters and LRDs, with flux normalized at 0.4 μm. The average SED of LRDs selected in the GOODS-S field presented in P. G. Pérez-González et al. (2024) is also included for comparison.

Overall, we do not observe significant differences between the average SEDs of our broad Hα emitters and LRDs within the rest-frame 0.1–1 μm range. The SEDs closely align up to rest-frame 0.4 μm, suggesting that LRDs may share similar UV emission properties with broad-line emitters. However, beyond 0.5 μm, the average SEDs of LRDs exhibit a noticeably steeper slope toward longer wavelengths compared to those of broad-line emitters, with particularly significant deviations at 0.5 and 0.65 μm. Given that the observed continuum in the average LRD SEDs between these wavelengths is comparable to that of broad-line emitters, we suspect that the steep red slope is not an intrinsic feature of at least some LRDs, but rather a result of line-boosting effects from strong emission lines, such as [O III] and Hα, falling within individual wide filters (K. N. Hainline et al. 2025). Figure 10 further supports the concern that adopting a low red slope cut for LRD selection may lead to contamination by sources that exhibit "fake" steep red slopes induced by such line-boosting effects, particularly when there are strong emission lines falling within the filters used for color selection.

5.5. Properties of Non-LRD AGN Galaxies

It should be noted that BLAGN galaxies that do not satisfy the NIRCam-based red slope criterion (and therefore drop out of the LRD selection) could still exhibit an SED upturn (i.e., a V-shaped SED) at $\lambda_{\rm obs} > 5\,\mu$m (i.e., beyond the NIRCam wavelength coverage). A good example is JADES 1089568 at $z = 4.05$ shown in the bottom panel of Figure 7. The figure shows that this object has a very blue color over the NIRCam passbands (e.g., due to its star-forming host), and in fact it is one of the bluest objects in Figure 9 in terms of the F277W − F444W color and $\beta_{\rm opt}$ slope. And yet it clearly exhibits a red SED rising beyond $\lambda_{\rm obs} \sim 5\,\mu$m ($\lambda_{\rm rest} \gtrsim 1\,\mu$m), which can be fit well with our AGN SED model. Such an SED is actually typical of AGN galaxies and widely seen across the redshift (e.g., J. Lyu et al. 2024) with hot dust emission from the AGN torus starting to dominate only in the rest-frame near/mid-infrared. This illustrates why the LRD selection (and more generally NIRCam-only color selections) is highly incomplete when selecting AGN galaxies (see also K. N. Hainline et al. 2025).

5.6. Detectability of Broad Hα Line in Grism Spectra

We identify 19 photometrically selected LRDs from P. Rinaldi et al. (2025a) that lie within the FRESCO and CONGRESS fields and have Hα emission detected in the grism spectra. However, 68% of these sources (13 out of 19) do not show broad Hα line profiles (i.e., FWHM < 1000 km s^{-1}) in the grism spectroscopy, with the exception of the six broad Hα emitters identified in this work. Such a low fraction of LRDs displaying broad-line features is consistent with the findings reported by P. G. Pérez-González et al. (2024).

Although no broad-line feature is observed in these LRDs, we cannot fully rule out the possibility that they are broad-line emitters, as the broad component could be hidden due to the insufficient sensitivity of the grism spectra. Notably, two sources that show no broad-line feature in the grism spectra have been reported to exhibit broad-line features in NIRSpec medium-resolution grating data in previous work (R. Maiolino et al. 2024). To illustrate how S/N may affect the detection of broad components, we present both the NIRSpec/grating and NIRCam/grism spectra for these two sources in Appendix C.

Figure 11 presents the distribution of our broad-line emitters and the photometrically selected LRDs of P. Rinaldi et al. (2025a), which lack broad-line features in the grism spectra, on the

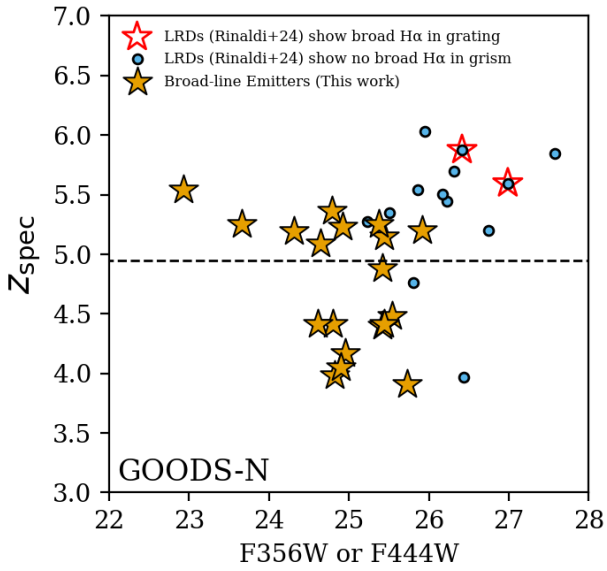

Figure 11. Distribution of broad Hα emitters (yellow stars) and photometrically selected LRDs (blue dots) from P. Rinaldi et al. (2025a) that show no broad Hα feature in grism spectra on the redshift–magnitude plane. The two blue dots enclosed by red stars represent LRDs exhibiting broad Hα emission in grating spectra but lacking such features in grism spectra. Sources below the dashed line have their Hα emission falling into the F356W band, so their F356W magnitudes are shown. Similarly, sources above the dashed line have their Hα emission in the F444W band, so their F444W magnitudes are shown.

redshift–magnitude plane. Overall, our broad-line emitters are significantly brighter than the LRDs, with a division at ∼26 mag that effectively separates the two populations. Notably, the two sources that exhibit broad-line features in the grating spectra but not in the grism are both fainter than 26 mag, suggesting that some faint LRDs may indeed be broad-line emitters, but their broad components are too faint to be detected in grism observations. In other words, the broad-line search with the CONGRESS/FRESCO data is effective only down to ∼26 mag.

6. Conclusion

In this study, we conduct a comprehensive spectroscopic search for broad Hα emitters at $z \approx 3.7-6.5$ in the GOODS-N field with JWST/NIRCam WFSS and imaging data. By combining photometric data from JADES with slitless spectroscopic observations from CONGRESS and FRESCO, we identify 19 broad Hα emitters at $z \approx 3.9-5.5$ with FWHM > 1000 km s^{-1}, including nine newly identified sources.

1. Among the 19 broad Hα emitters, 18 have a broad component that contributes more than 50% of the total Hα flux. Additionally, the [O III] λ5007 emission line is detected in three sources, with line widths significantly narrower than those of the broad Hα components, suggesting that the observed broad features of these sources are mainly driven by the AGN BLR. By computing the broad Hα LF of our sample, we find that it is consistent with those of other JWST-selected BLAGN in the literature.
2. We derive black hole masses and AGN bolometric luminosities for our sample based on the measured FWHMs and line fluxes of the broad Hα components. Most sources are found to be accreting at ∼10% of the Eddington limit, consistent with the accretion rates of BLAGN selected with NIRSpec in other studies.
3. The stellar masses of the host galaxies in our sample are derived through SED fitting using `Prospector`. Consistent with previous studies, our sample exhibits higher $M_{\rm BH}/M_*$ ratios relative to the local $M_{\rm BH}-M_*$ relations reported by A. E. Reines & M. Volonteri (2015) and J. E. Greene et al. (2020). However, given that our sample is selected based on the detection of broad Hα emission, some degree of selection bias may be present. In particular, low-$M_{\rm BH}$ sources may be missed due to the limited sensitivity of the grism, which could prevent the detection of faint broad-line components.
4. By testing various LRD selection techniques proposed in the literature, we find that all of these methods will miss a significant fraction of our spectroscopically confirmed broad Hα emitters, while the majority of the broad Hα emitters that fail the LRD color selection lack steep red slopes. This suggests that not all broad-line emitters with a compact and red appearance exhibit the characteristic "V-shaped" SEDs of LRDs.
5. To further investigate the nature of LRDs, we compare the average SED of our broad-line emitter sample with that of the photometrically selected LRDs from P. Rinaldi et al. (2025a) in the same field. The average SEDs are largely consistent with each other, except for a steeper red slope in the LRD sample at rest-frame wavelength >0.5 μm, likely due to the contribution of [O III] and Hα emission. Given the much lower continuum levels observed between these two lines, we conclude that the red slope, at least in some LRDs, would be naturally less steep if emission lines are removed, as discussed in K. N. Hainline et al. (2025).
6. We further examine the LRDs in the GOODS-N field with Hα detections in the grism spectra and find that ∼68% do not exhibit broad Hα features. This suggests that the LRD population may not only consist of broad-line emitters. Additionally, we identify two LRDs that lack broad Hα features in the NIRCam grism spectra but do show broad components in the NIRSpec grating spectra. Both of these sources are fainter than 26 mag in the filter where Hα is observed, whereas the majority of our broad Hα emitters are brighter than this threshold. This implies that the broad-line search with the CONGRESS/FRESCO data is effective only down to ∼26 mag, and therefore some LRDs may indeed host broad-line components that are undetected in the grism data due to its limited sensitivity.

This work identifies an abundant population of broad Hα emitters in the GOODS-N field at $3.9 < z < 5.5$, providing a valuable sample for studying the abundance and properties of broad Hα emitters in the early Universe. Our results also highlight the strong selection capabilities of grism spectroscopy and offer insights into the brightness threshold required for detecting broad Hα emitters with grisms. Future follow-up observations with NIRSpec will be crucial for confirming the nature of these sources and further characterizing this population.

Acknowledgments

E.E. and Y.Z. acknowledge support from the NIRCam Science Team contract to the University of Arizona, NAS 5-02105. A.J.B. acknowledges funding from the "FirstGalaxies" Advanced Grant from the European Research Council (ERC) under the European Union's Horizon 2020 research and

innovation program (grant agreement No. 789056). R.M. acknowledges support by the Science and Technology Facilities Council (STFC), by the ERC through Advanced Grant 695671 "QUENCH," and by the UKRI Frontier Research grant RISEandFALL. R.M. also acknowledges funding from a research professorship from the Royal Society. B.R. acknowledges support from the NIRCam Science Team contract to the University of Arizona, NAS 5-02105, and JWST Program 3215. S.T. acknowledges support by the Royal Society Research Grant G125142. G.V. acknowledges support by the European Union's HE ERC Starting Grant No. 101040227—WINGS. The research of C.C.W. is supported by NOIRLab, which is managed by the Association of Universities for Research in Astronomy (AURA) under a cooperative agreement with the National Science Foundation.

This work is based on observations made with the NASA/ESA Hubble Space Telescope and NASA/ESA/CSA James Webb Space Telescope. The data were obtained from the Mikulski Archive for Space Telescopes at the Space Telescope Science Institute, which is operated by the Association of Universities for Research in Astronomy, Inc., under NASA contract NAS 5-03127 for JWST. These observations are associated with program #1181 (JADES), #1895 (FRESCO), and #3577 (CONGRESS). The specific JWST observations analyzed can be accessed via DOI:10.17909/6rfk-6s81. Support for program #3577 was provided by NASA through a grant from the Space Telescope Science Institute, which is operated by the Association of Universities for Research in Astronomy, Inc., under NASA contract NAS 5-03127. The authors thank the FRESCO team for developing their observing program with a zero-exclusive-access period.

Appendix A
Nonconfirmation of Two Broad Hα Emitters Reported by A. Covelo-Paz et al. (2025)

In our sample, we exclude two broad Hα emitters reported by A. Covelo-Paz et al. (2025) due to concerns regarding the validity of their classification. For the first source (JADES ID: 1080661; R.A. = 189°.27616, decl. = 62°.21416), the flux ratio $\frac{F(\mathrm{F444W})r=0\farcs3}{F(\mathrm{F444W})r=0\farcs1} \approx 2.1$ does not meet our compactness criterion. Given that the selection criteria in A. Covelo-Paz et al. (2025) do not incorporate compactness, this mismatch is natural. Figure 12 presents the 1D and 2D grism spectra obtained in F356W from CONGRESS. The F356W direct image reveals an extended morphology for this source. We also perform a 1D line fit of its Hα line profile. As illustrated in Figure 13, even after accounting for potential morphological broadening, the best-fit FWHM is only $\sim$500 km s^{-1}, which does not satisfy our requirement for the line width of a broad Hα emitter. Additionally, we note that our best-fit FWHM differs from the value reported in A. Covelo-Paz et al. (2025) (i.e., 1674 km s^{-1}). However, the cause of this discrepancy is unclear.

For the second source (JADES ID: 1089616; R.A. = 189°.18713, decl. = 62°.27289), the top right panels of Figure 14 show its 1D and 2D grism spectra in F356W from CONGRESS. While a strong emission feature is detected at 3.8 μm, we observe a noticeable spatial offset between the position of the emission line and that of the source in the direct image, raising concerns about its association with the target. In the bottom panels of Figure 14, which present the F444W grism spectra from FRESCO for the same source, an emission line at $\sim$4.15 μm is detected with no spatial offset and a S/N $\sim$ 4. Combined with the detection of another emission line at $\sim$3.17 μm, we identify these features as Hα and [O III] λ5007 of this source, respectively, confirming the redshift of the source is 5.324. The relatively weak line strengths are also consistent with the faint nature of the source in the direct images. Upon further inspection, the strong 3.8 μm line is confirmed to be [S III] λ9531 from a nearby bright source (JADES ID: 1029833; R.A. = 189°.20103, decl. = 62°.26567). Figure 15 presents the 1D and 2D grism spectra of this source in the F356W and F444W filters. The [S III] λ9531 emission line of this source matches the 3.8 μm emission line observed in the 2D spectrum of source 1089616 very well, suggesting the 3.8 μm emission line is not Hα of 1089616, but [S III] λ9531 of 1029833.

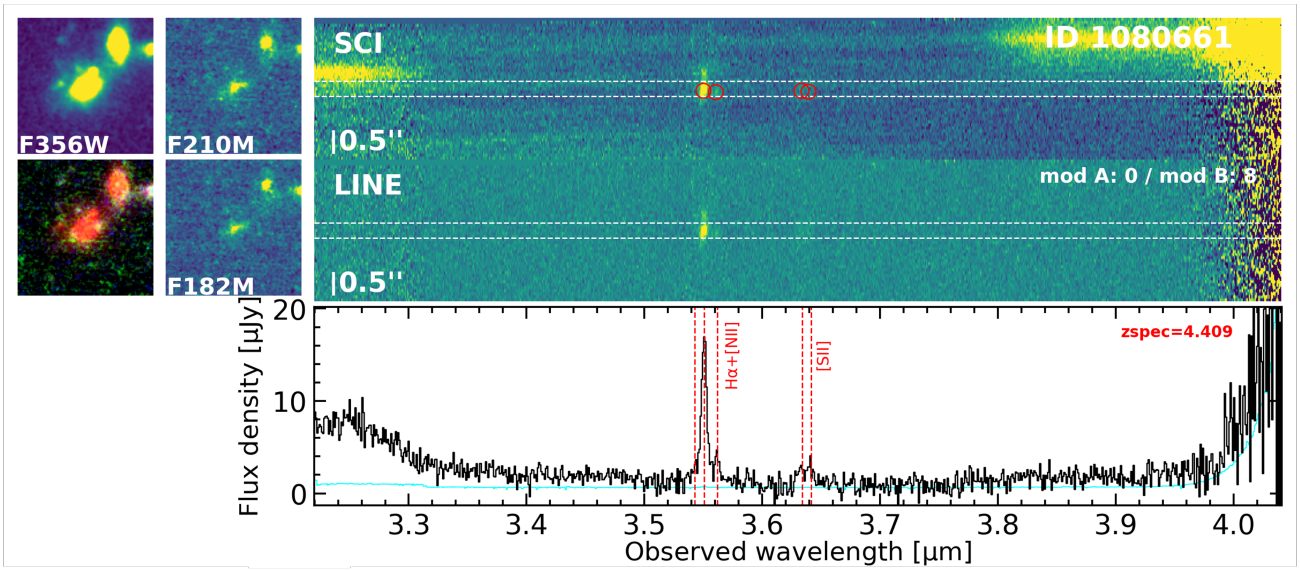

Figure 12. 2D and 1D grism spectra of 1080661 obtained in the F356W filter from CONGRESS. Top right: 2D spectrum with continuum; red empty circles indicate detected lines. Middle right: line-only 2D spectrum. Bottom right: optimally extracted 1D spectrum with continuum. Emission lines detected are marked by red dashed lines. The top left corner displays direct images of the source in the F182M, F210M, and F356W filters, along with a composite false-color stamp constructed from these three bands.

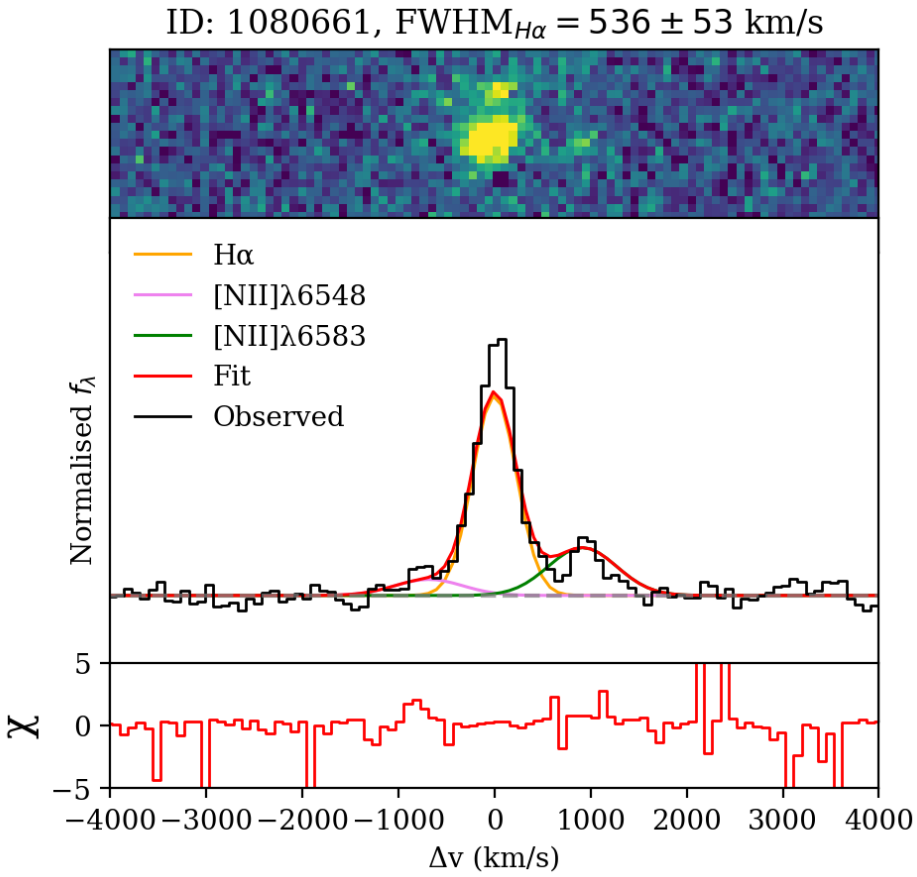

Figure 13. 1D line fitting results for the Hα emission profile of 1080661. Top panel: 2D grism spectrum with continuum subtracted. Middle panel: optimally extracted 1D grism spectrum (black); the red line represents the best-fit model. The yellow, pink, and green lines correspond to the Hα, [N II] λ6548, and [N II] λ6583 components, respectively. Bottom panel: residuals from the best-fit model.

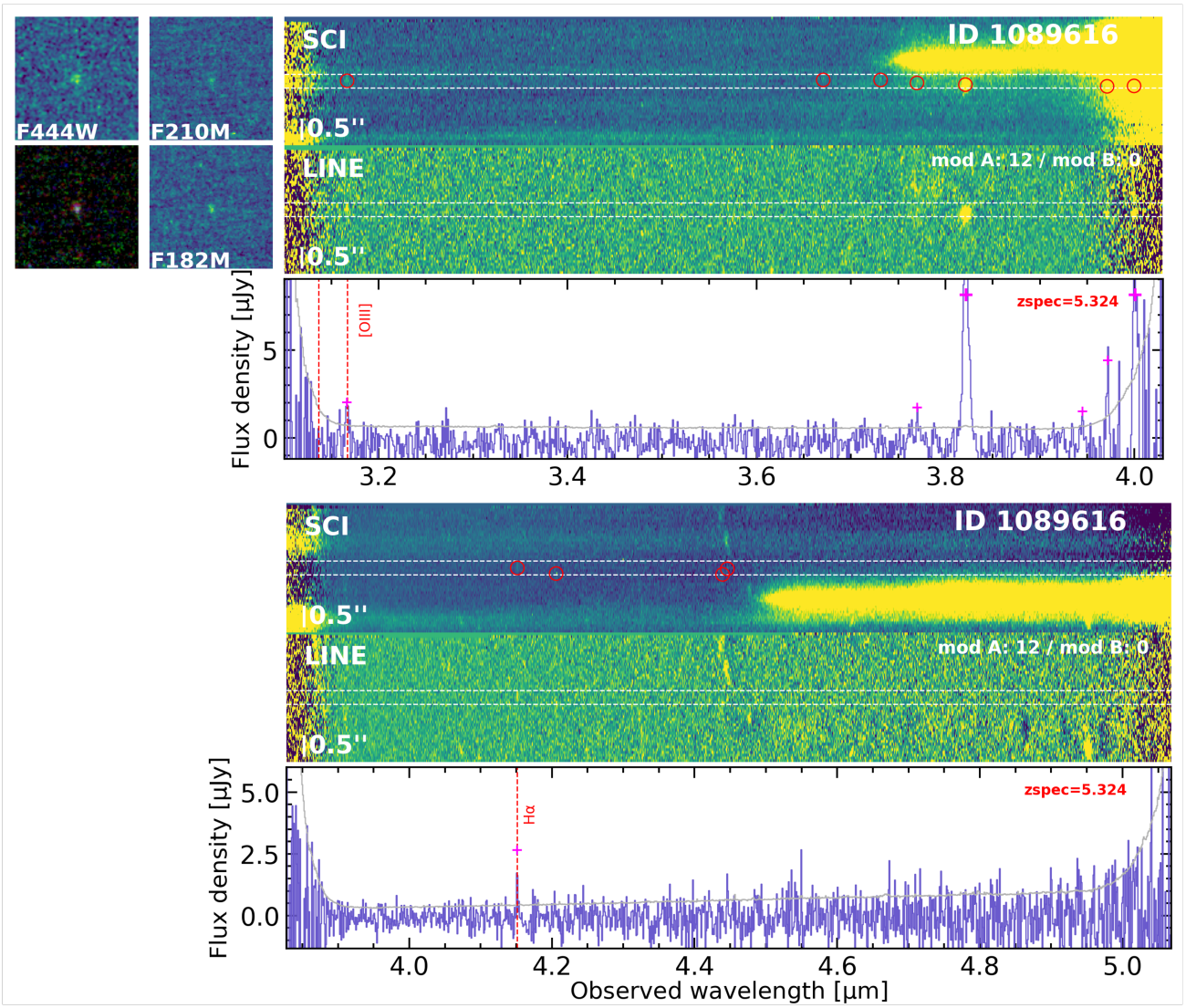

Figure 14. 2D and 1D grism spectra of 1089616 obtained in the F356W (top right panels) and F444W (bottom right panels) filters from CONGRESS and FRESCO, respectively. Top subpanels: 2D spectrum with continuum; red empty circles indicate detected lines. Middle subpanels: median-filtered line-only 2D spectrum. Bottom subpanels: optimally extracted 1D spectrum from the line-only 2D spectrum, with detected emission lines marked by red dashed lines. The top left corner displays direct images of the source in the F182M, F210M, and F444W filters, along with a composite false-color stamp constructed from these three bands.

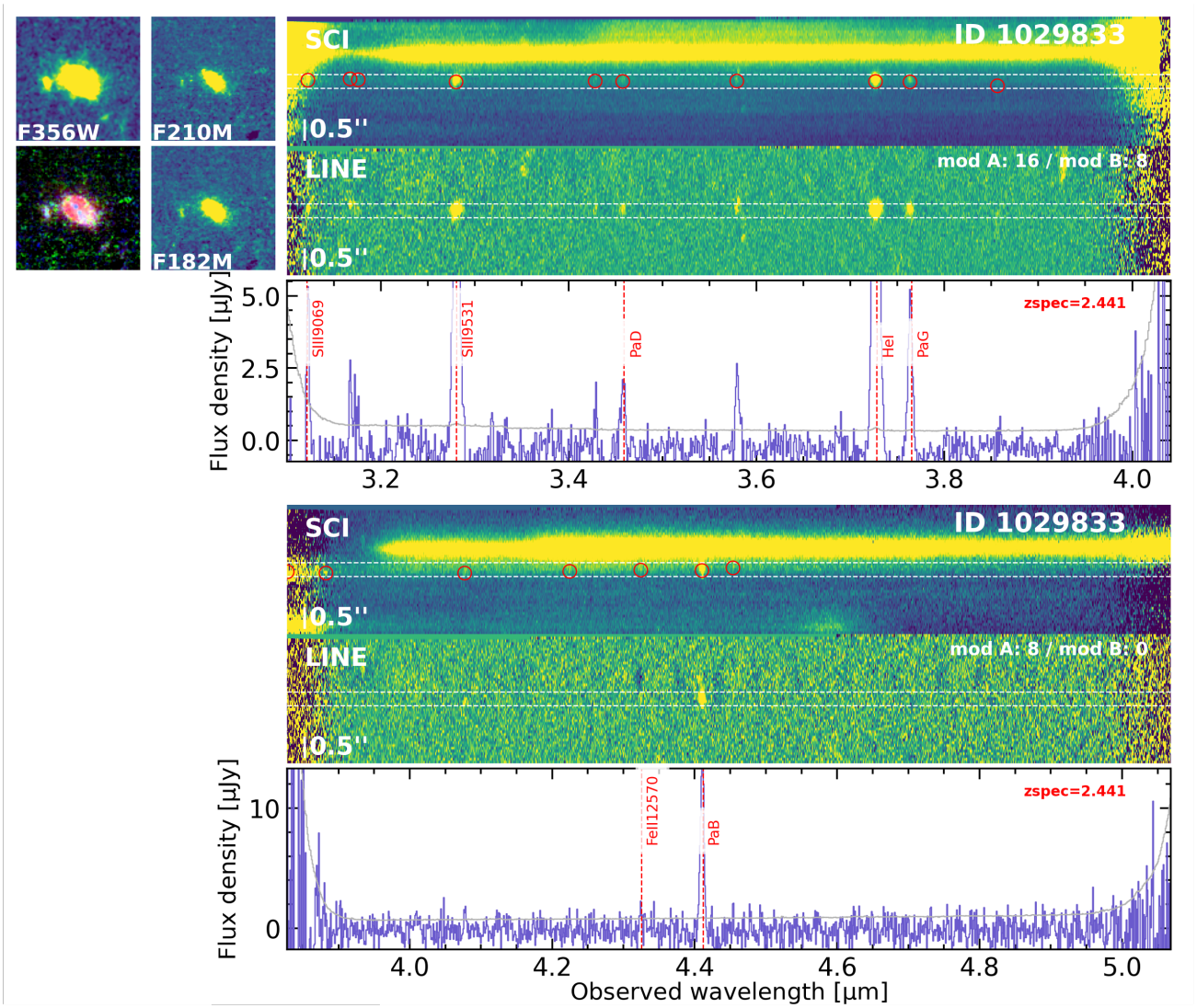

Figure 15. 2D and 1D NIRCam/grism spectra of 1029833 obtained in the F356W (top right panels) and F444W (bottom right panels) filters from CONGRESS and FRESCO, respectively. Top subpanels: 2D spectrum with continuum; red empty circles indicate detected lines. Middle subpanels: median-filtered line-only 2D spectrum. Bottom subpanels: optimally extracted 1D spectrum from the line-only 2D spectrum, with detected emission lines marked by red dashed lines. The top left corner displays direct images of the source in the F182M, F210M, and F444W filters, along with a composite false-color stamp constructed from these three bands.

Appendix B
Discrepant Broad-line Widths for a BLAGN Reported by J. E. Greene et al. (2024)

Recently, the JWST Cycle 3 General Observer program Slitless Areal Pure-parallel High-redshift Emission Survey (SAPPHIRES-PID: 6434; PI: E. Egami; F. Sun et al. 2025) revisited the A2744 field and obtained a NIRCam grism spectrum ($R \sim 1600$) for one of the BLAGN (Prism ID: 38108; SAPPHIRES ID: 39082) identified in J. E. Greene et al. (2024). Figure 16 shows the observed Hα line in 1D and 2D grism spectra obtained in the F444W filter, along with the line fitting results. The 1D grism spectrum reveals a broad Hα component with a line width of $\sim$1300 km s^{-1}, which contrasts significantly with the prism-based value of $\sim$4000 km s^{-1}. For comparison, we also include the Hα broad component observed in prism by using the FWHM and Hα flux (treated as an upper limit of the flux for the broad component) reported by J. E. Greene et al. (2024). Even a modest difference in the FWHM measurements can result in a substantial variation in the inferred $M_{\rm BH}$. In Figure 6, we plot the AGN bolometric luminosity and black hole mass derived for this source from the SAPPHIRES NIRCam grism data (the "X" marker). With the smaller $M_{\rm BH}$ inferred from the grism spectrum, the source becomes more consistent with the distribution of our sample, providing a potential explanation for the discrepancy in black hole mass estimates.

However, the underlying cause of the discrepancy in FWHM measurements remains unclear. Taking into account the large uncertainty associated with the prism-based FWHM, our measurement and that from J. E. Greene et al. (2024) are broadly consistent with each other at the 2σ level. Since our line fitting is performed on spectra without continuum subtraction, we can rule out the possibility that the broad component is lost due to oversubtraction of continuum. There are two possible explanations for this discrepancy. First, the difference in FWHM values may arise from differences in the respective LSFs. Second, the grism observation may lack the sensitivity required to detect such a faint broad component. Furthermore, we note that J. E. Greene et al. (2024) identified broad-line sources using slightly different selection criteria, in

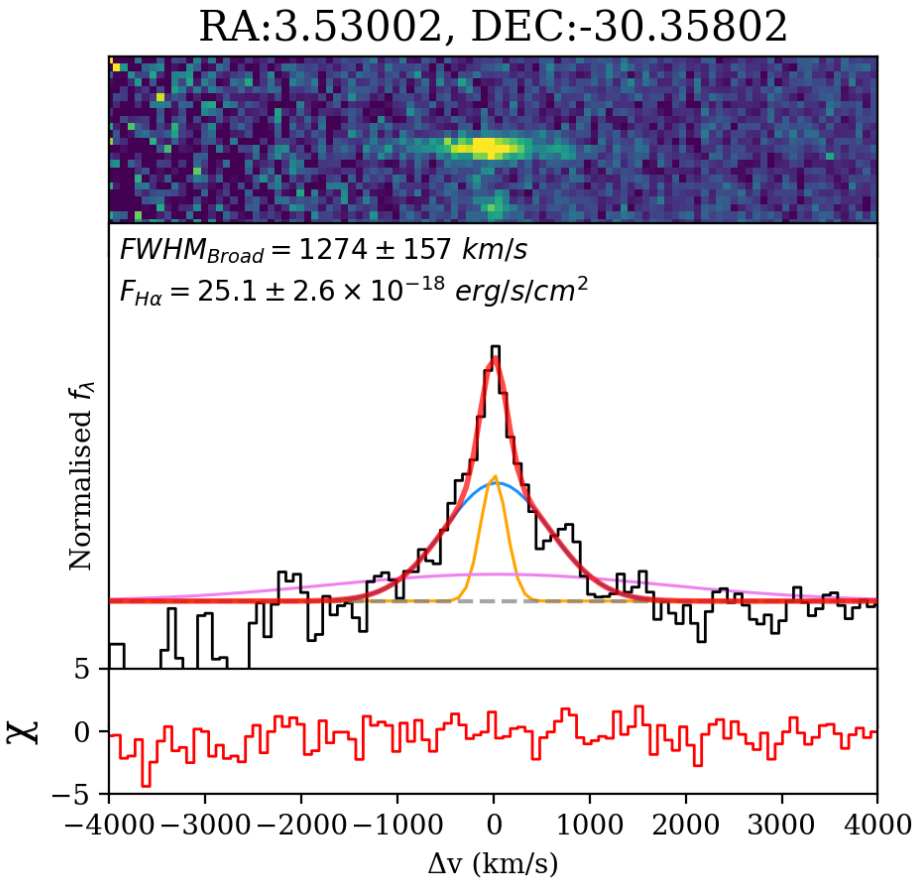

Figure 16. Multicomponent Gaussian fit to the Hα line profile in the NIRCam/grism spectrum ($R \sim 1600$) for a BLAGN previously identified with the NIRSpec/prism in J. E. Greene et al. (2024). Top panel: 2D grism spectrum without continuum subtraction. Middle panel: optimally extracted 1D spectrum (black), best-fit model (red), and individual components: narrow Hα (yellow) and broad Hα (blue). The pink line represents the broad component observed with the prism, using the FWHM and Hα flux (treated as an upper limit of the flux for the broad component) reported by J. E. Greene et al. (2024). The intrinsic FWHM of the broad component and the observed Hα flux are indicated in the top left corner. Bottom panel: residuals from the multicomponent fit.

particular requiring the FWHM of the broad Hα component to be $>2000\,\mathrm{km\,s^{-1}}$. This difference in criteria may also contribute to the discrepancy in FWHM measurements.

Appendix C
NIRSpec Medium Grating versus NIRCam Grism

In this work, we identify two photometrically selected LRDs from P. Rinaldi et al. (2025a) that exhibit broad Hα line profiles in the NIRSpec medium-resolution grating spectra presented by R. Maiolino et al. (2024), but not in the NIRCam grism spectra, likely due to the limited sensitivity of the grism observations. Figure 17 illustrates the differences in the observed Hα line profiles for these two sources between the grism and grating data. The S/N of the grating spectra are slightly lower than those presented in R. Maiolino et al. (2024), possibly due to differences in the spectrum extraction methods. In both cases, the Hα lines appear significantly narrower in the grism spectra compared to the grating spectra. Additionally, the grism continuum exhibits a much higher noise level, supporting the possibility that the broad components are undetected due to the lower S/N of the grism observations.

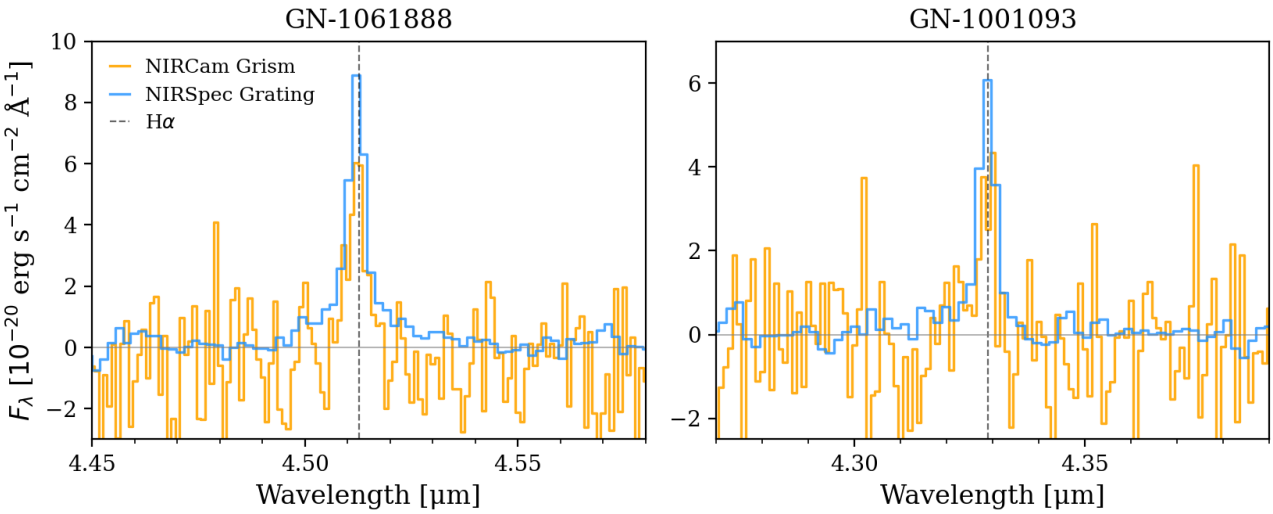

Figure 17. Comparison of the Hα line profiles for two LRDs identified in P. Rinaldi et al. (2025a), as observed from NIRCam grism (orange) and NIRSpec grating (blue) spectra. The dashed gray line marks the centroid wavelength of Hα.

ORCID iDs

Junyu Zhang https://orcid.org/0000-0002-1574-2045
Eiichi Egami https://orcid.org/0000-0003-1344-9475
Fengwu Sun https://orcid.org/0000-0002-4622-6617
Xiaojing Lin https://orcid.org/0000-0001-6052-4234
Jianwei Lyu https://orcid.org/0000-0002-6221-1829
Yongda Zhu https://orcid.org/0000-0003-3307-7525
Pierluigi Rinaldi https://orcid.org/0000-0002-5104-8245
Yang Sun https://orcid.org/0000-0001-6561-9443
Andrew J. Bunker https://orcid.org/0000-0002-8651-9879
Rachana Bhatawdekar https://orcid.org/0000-0003-0883-2226
Jakob M. Helton https://orcid.org/0000-0003-4337-6211
Roberto Maiolino https://orcid.org/0000-0002-4985-3819
Zheng Ma https://orcid.org/0009-0003-5402-4809
Brant Robertson https://orcid.org/0000-0002-4271-0364
Sandro Tacchella https://orcid.org/0000-0002-8224-4505
Giacomo Venturi https://orcid.org/0000-0001-8349-3055
Christina C. Williams https://orcid.org/0000-0003-2919-7495
Chris Willott https://orcid.org/0000-0002-4201-7367

References

Akins, H. B., Casey, C. M., Allen, N., et al. 2023, ApJ, 956, 61
Barro, G., Pérez-González, P. G., Kocevski, D. D., et al. 2024, ApJ, 963, 128
Bogdán, Á., Goulding, A. D., Natarajan, P., et al. 2024, NatAs, 8, 126
Conroy, C., & Gunn, J. E. 2010, ApJ, 712, 833
Conroy, C., Gunn, J. E., & White, M. 2009, ApJ, 699, 486
Covelo-Paz, A., Giovinazzo, E., Oesch, P. A., et al. 2025, A&A, 694, A178
de Graaff, A., Rix, H.-W., Naidu, R. P., et al. 2025, A&A, 701, A168
D'Eugenio, F., Cameron, A. J., Scholtz, J., et al. 2025a, ApJS, 277, 4
D'Eugenio, F., Maiolino, R., Perna, M., et al. 2025b, arXiv:2503.11752
Dojčinović, I., Kovačević Dojčinović, J., & Popović, L. Č. 2023, AdSpR, 71, 1219
Eisenstein, D. J., Willott, C., Alberts, S., et al. 2023, arXiv:2306.02465
Finkelstein, S. L., & Bagley, M. B. 2022, ApJ, 938, 25
Gaia Collaboration, Vallenari, A., Brown, A. G. A., et al. 2023, A&A, 674, A1
Gardner, J. P., Mather, J. C., Abbott, R., et al. 2023, PASP, 135, 068001
Giallongo, E., Grazian, A., Fiore, F., et al. 2019, ApJ, 884, 19
Giavalisco, M., Ferguson, H. C., Koekemoer, A. M., et al. 2004, ApJL, 600, L93
Greene, J. E., & Ho, L. C. 2005, ApJ, 630, 122
Greene, J. E., Labbe, I., Goulding, A. D., et al. 2024, ApJ, 964, 39
Greene, J. E., Strader, J., & Ho, L. C. 2020, ARA&A, 58, 257
Hainline, K. N., Maiolino, R., Juodžbalis, I., et al. 2025, ApJ, 979, 138
Harikane, Y., Zhang, Y., Nakajima, K., et al. 2023, ApJ, 959, 39
Horne, K. 1986, PASP, 98, 609
Hviding, R. E., de Graaff, A., Miller, T. B., et al. 2025, A&A, 702, A57
Ji, X., Maiolino, R., Übler, H., et al. 2025, MNRAS, 544, 3900
Johnson, B., Leja, J., Bowman, W., et al. 2022, bd-j/prospector: v1.1, v1.1.0, Zenodo, doi:10.5281/zenodo.6192136
Johnson, B. D., Leja, J., Conroy, C., & Speagle, J. S. 2021, ApJS, 254, 22
Juodžbalis, I., Ji, X., Maiolino, R., et al. 2024, MNRAS, 535, 853
Juodžbalis, I., Maiolino, R., Baker, W. M., et al. 2025, arXiv:2504.03551
Kocevski, D. D., Finkelstein, S. L., Barro, G., et al. 2025, ApJ, 986, 126
Kocevski, D. D., Onoue, M., Inayoshi, K., et al. 2023, ApJL, 954, L4
Koekemoer, A. M., Faber, S. M., Ferguson, H. C., et al. 2011, ApJS, 197, 36
Kokorev, V., Caputi, K. I., Greene, J. E., et al. 2024, ApJ, 968, 38
Kormendy, J., & Ho, L. C. 2013, ARA&A, 51, 511
Labbé, I., Greene, J. E., Bezanson, R., et al. 2025, ApJ, 978, 92
Larson, R. L., Finkelstein, S. L., Kocevski, D. D., et al. 2023, ApJL, 953, L29
Leja, J., Johnson, B. D., Conroy, C., van Dokkum, P. G., & Byler, N. 2017, ApJ, 837, 170
Liddle, A. R. 2007, MNRAS, 377, L74
Lin, X., Egami, E., Sun, F., et al. 2025a, arXiv:2504.08028
Lin, X., Fan, X., Cai, Z., et al. 2025b, arXiv:2507.10659
Lin, X., Fan, X., Sun, F., et al. 2025c, arXiv:2505.02896
Lin, X., Fan, X., Wang, F., et al. 2026, ApJ, 996, 93
Lin, X., Wang, F., Fan, X., et al. 2024, ApJ, 974, 147
Lyu, J., Alberts, S., Rieke, G. H., et al. 2024, ApJ, 966, 229
Maiolino, R., Scholtz, J., Curtis-Lake, E., et al. 2024, A&A, 691, A145
Matthee, J., Naidu, R. P., Brammer, G., et al. 2024, ApJ, 963, 129
Morishita, T., Stiavelli, M., Trenti, M., et al. 2020, ApJ, 904, 50
Naidu, R. P., Matthee, J., Katz, H., et al. 2025, arXiv:2503.16596
Noboriguchi, A., Nagao, T., Toba, Y., et al. 2019, ApJ, 876, 132
Oesch, P. A., Brammer, G., Naidu, R. P., et al. 2023, MNRAS, 525, 2864
Oke, J. B., & Gunn, J. E. 1983, ApJ, 266, 713
Parsa, S., Dunlop, J. S., & McLure, R. J. 2018, MNRAS, 474, 2904
Pérez-González, P. G., Barro, G., Rieke, G. H., et al. 2024, ApJ, 968, 4
Reines, A. E., Greene, J. E., & Geha, M. 2013, ApJ, 775, 116
Reines, A. E., & Volonteri, M. 2015, ApJ, 813, 82
Richards, G. T., Lacy, M., Storrie-Lombardi, L. J., et al. 2006, ApJS, 166, 470
Rieke, M., Robertson, B., Tacchella, S., et al. 2023, Data from the JWST Advanced Deep Extragalactic Survey (JADES), DR2, STScI/MAST, doi:10.17909/8TDJ-8N28
Rinaldi, P., Bonaventura, N., Rieke, G., et al. 2025a, ApJ, 992, 71
Rinaldi, P., Pérez-González, P. G., Rieke, G. H., et al. 2025b, ApJ, 994, 86
Rusakov, V., Watson, D., Nikopoulos, G. P., et al. 2025, arXiv:2503.16595
Schmidt, M. 1968, ApJ, 151, 393
Schneider, R., Valiante, R., Trinca, A., et al. 2023, MNRAS, 526, 3250

Shen, X., Hopkins, P. F., Faucher-Giguère, C.-A., et al. 2020, MNRAS, 495, 3252
Sun, F., Egami, E., Pirzkal, N., et al. 2023, ApJ, 953, 53
Sun, F., Fudamoto, Y., Lin, X., et al. 2025, arXiv:2503.15587
Sun, Y., Lyu, J., Rieke, G. H., et al. 2025a, ApJ, 978, 98
Sun, Y., Rieke, G. H., Lyu, J., et al. 2025b, ApJ, 983, 165
Trinca, A., Schneider, R., Valiante, R., et al. 2022, MNRAS, 511, 616
Übler, H., Maiolino, R., Curtis-Lake, E., et al. 2023, A&A, 677, A145
Volonteri, M., Habouzit, M., & Colpi, M. 2023, MNRAS, 521, 241
Williams, C. C., Alberts, S., Ji, Z., et al. 2024, ApJ, 968, 34
Yang, J., Wang, F., Fan, X., et al. 2021, ApJ, 923, 262
Zhu, Y., Rieke, M. J., Ho, L. C., et al. 2025, arXiv:2504.02305